

A new method to obtain the Broad Line Region size of high redshift quasars ♣

C. Alenka Negrete

Instituto Nacional de Astrofísica, Óptica y Electrónica, Mexico

cnegrete@inaoep.mx

Deborah Dultzin

Instituto de Astronomía, Universidad Nacional Autónoma de México, Mexico

deborah@astro.unam.mx

Paola Marziani

INAF, Astronomical Observatory of Padova, Italy

paola.marziani@oapd.inaf.it

and

Jack W. Sulentic

Instituto de Astrofísica de Andalucía, Spain

sulentic@iaa.es

ABSTRACT

We present high S/N UV spectra for eight quasars at $z \sim 3$ obtained with VLT/FORS. The spectra enable us to analyze in detail the strong and weak emission features in the rest-frame range 1300-2000 Å of each source (CIII]λ1909, SiIII]λ1892, AlIIIλ1860, SiIIλ1814, CIVλ1549 and blended SiIVλ1397+OIV]λ1402). Flux ratios AlIIIλ1860/SiIII]λ1892, CIVλ1549/AlIIIλ1860, SiIVλ1397+OIV]λ1402/SiIII]λ1892 and SiIVλ1397+OIV]λ1402/CIVλ1549 strongly constrain ionizing photon flux

⁰Based on observations made with ESO Telescopes at Paranal Observatory under programme ID 078.B-0109(A)

and metallicity through the use of diagnostic maps built from CLOUDY simulations. The radius of the broad line region is then derived from the ionizing photon flux applying the definition of the ionization parameter. The r_{BLR} estimate and the width of a virial component isolated in prominent UV lines yields an estimate of black hole mass. We compare our results with previous estimates obtained from the $r_{\text{BLR}} - \text{luminosity}$ correlation customarily employed to estimate black hole masses of high redshift quasars.

Subject headings: galaxies: active — galaxies: high-redshift — quasars: general — quasars: emission lines

1. Introduction

Measuring relevant physical parameters from the observed broad-line spectra of quasars is still an open challenge. Identification and intensity measurements of the strongest emission lines has made possible a rough inference about typical conditions in the emitting gas from the earliest days of quasar spectroscopy. The first intermediate redshift quasars discovered in the 1960s showed a fairly high ionization spectrum with prominent lines of C IV $\lambda 1549$, and He II $\lambda 1640$ in addition to strong Balmer lines seen in the lower redshift sources. Photoionization by a central continuum source was considered the principal heating mechanism of the emitting gas. Significant C III] $\lambda 1909$ emission suggested electron densities (n_e) in the range $10^9 - 10^{10} \text{ cm}^{-3}$. The observed intensity ratio C III] $\lambda 1909$ /C IV $\lambda 1549$ indicated ionization parameter (U ; defined by Eq. 1 later in this paper) values of the order of 10^{-1} . This photoionization scenario was successful in explaining at least some quasar optical and UV spectra (see the review by Davidson & Netzer 1979 for a synopsis).

More recent work recognized the existence of several problems with the original scenario. Low ionization lines (LILs), and especially Fe II are too strong to be explained by a photoionized region of moderate density and column density (see for example Dumont & Mathez 1981; Joly 1987; Collin-Souffrin et al. 1988; Collin-Souffrin & Dumont 1990). These authors stressed that the LILs required a denser, low-temperature environment. Even more recently, Baldwin et al. (1996); Laor et al. (1997a); Baldwin et al. (2004) point towards high density at least for the LIL emitting zone. This low ionization broad line region (LIL BLR) has very similar properties to the O I and Ca II emitting region identified by Matsuoka et al. (2008). The region where these LILs are produced cannot emit much C III] $\lambda 1909$ if the electron density exceeds 10^{11} cm^{-3} . BLR conditions are certainly complex and the assumption of a single emitting region cannot explain both LILs and high ionization lines (HILs) in all quasars (Marziani et al. 2010; Wang et al. 2011, and references therein).

In Negrete et al. (2012), hereafter Paper I, we report an analysis based on several diagnostic ratios used to constrain density, ionization parameter and metallicity in the BLR of two sources that are representative of extreme Population A (narrow Line Seyfert 1 - NLSy1) sources. These sources showed weak CIII] λ 1909 emission (relative to SiIII] λ 1892) which simplified our interpretation of the emission line spectra. Diagnostic ratios indicate a very dense ($n_e \sim 10^{12} \text{ cm}^{-3}$), low ionization ($U \sim 10^{-2.7}$) region that, in a photoionization scenario, is expected to also emit FeII and CaII lines (e.g., Brühweiler & Verner 2008; Matsuoka et al. 2008). In Negrete et al. (2013), hereafter Paper II, we show that CIII] λ 1909 is not associated with the high density region. However CIII] λ 1909 is strong in most sources, dominating the emission of the 1900Å blend. The presence of strong CIII] λ 1909 indicates that the BLR cannot be characterized anymore by a narrow range of density and ionization parameter: a gradient of ionization, of density, or both may be present. Since the BLR is not spatially resolved, the meaning of emission line ratios becomes much more ambiguous, and we cannot obtain meaningful single-value measures of n_H and ionization. Nonetheless, the ionizing photon flux (i.e., the product $n_H U$) can be retrieved with an accuracy comparable to estimates obtained from reverberation mapping, and then used to estimate r_{BLR} (Paper II).

In this paper we apply the method discussed in Paper II to a pilot sample of high redshift ($z \sim 3$) sources. The technique we present should allow one to easily compute r_{BLR} for large samples of high z sources. Moderate resolution and high S/N dedicated observations allowed us to detect and measure faint and blended lines in order to analyze all physical information that can be retrieved from rest frame UV spectra of high- z quasars. The pilot sample helps us to explore challenges that exist for studying high- z sources using only rest-frame UV spectra. Estimation of redshift cannot rely on measures of low-ionization narrow lines that are the most credible diagnostics at low z . (Eracleous & Halpern 2003; Hu et al. 2008). Narrow lines are weak and often undetectable in very high luminosity sources (Marziani et al. 2009), a phenomenon sometimes called the [OIII] $\lambda\lambda$ 4959,5007 Baldwin effect; Zhang et al. 2011). On the other hand, the criteria for population and spectral type identification were set from properties of the H β spectral range (Sulentic et al. 2000) that is customarily not available for high z quasars.

We present the spectra of 8 pilot sources obtained with the VLT/FORS1 in Section 2; Section 3 summarizes data reduction including details of redshift estimation (Section 3.2). Before discussing the analysis of the data, we present a synopsis of quasar systematics along the so-called “eigenvector 1” (E1), with special attention on the interpretation of the line profiles. In Section 4 we apply the interpretation of the line profiles derived from low- z sources to fit the line profiles in this high z sample. In Section 5 we discuss the population assignment and the properties of each source, while Section 6 explores BLR physical conditions, with special reference to metallicity issues (Section 6.3). Section 7

presents results from application of the photoionization method to our pilot sample. Section 8 presents derivations of the BLR radius (r_{BLR} ; its distance from the ionizing source) and black hole mass (M_{BH}). Section 9 compares our results with previous work and Section 10 considers the prospects for application of our technique for single epoch M_{BH} estimates in high redshift samples. All the computations were made considering $H_0 = 70 \text{ km s}^{-1} \text{ Mpc}^{-1}$ and relative energy densities $\Omega_{\Lambda} = 0.7$ and $\Omega_{\text{M}} = 0.3$.

2. Observations

Data were obtained between Nov. 2006 and Jan. 2007 using the VLT2/FORS1 telescope operated in service mode. FORS1 is the visual and near UV focal reducer and low dispersion spectrograph of the Very Large Telescope (VLT) operated by European Southern Observatory (ESO; Appenzeller et al. 1998). A pilot sample of 8 quasars at $z \sim 3$ was observed with long exposure times to ensure high S/N in the continuum, in all cases above ≈ 40 , and otherwise in the range 50 – 100. Table 1 provides a log of observations that is organized as follows: Column (1) object name, Col. (2) apparent B magnitude, Col. (3) redshift, Col. (4) redshift uncertainty, Col. (5) line used for redshift estimation: 1) OI λ 1304, 2) CIII] λ 1909; Col. (6) absolute B magnitude, Col. (7) flux at 6 cm taken from FIRST (Becker et al. 1995), Col. (8) date (refers to time at start of exposure), Col. (9) Digital Integration Time, Col. (10) number of exposures with integration time equal to DIT, Col. (11) average of the airmass, Col. (12) S/N in the continuum around 1700Å.

The observation of one of our 8 quasars, J00521-1108, yielded the lowest S/N spectrum which we retain because observed features in the blend at $\sim 1900\text{Å}$ are clear enough to fit the individual lines. Two sources, J01225+1339 and J02287+0002, are high-ionization broad absorption lines (BAL) quasars with deep absorption troughs deeply affecting the CIV λ 1549 emission profile.

3. Data Reduction

Data were reduced using standard IRAF tasks. All spectra were wavelength and flux calibrated in the observed frame and then corrected for Galactic extinction. Flux correction was applied using meteorological data provided by ESO. The observed flux was multiplied by the inverse of the light lost computed from the ratio seeing over slit width in arcsec. Correction to rest frame requires estimating the redshift z which is not a trivial task as outlined below. Rest frame correction also involved scaling the specific flux in flux per unit

wavelength interval by a factor $(1 + z)^3$. Measurements were carried out on the rest-frame spectra. It is necessary to describe below two important aspects of the data reduction.

3.1. A & B Atmospheric Bands Correction

The A or B atmospheric band falls on top of the 1900Å blend in many of the spectra. This is an important region for this study especially because it involves SiIII]λ1892, AlIIIλ1860, and SiIIλ1814. In order to remove these absorption features we created an A+B band template from standard star spectra used as specific flux calibrators. We scaled this template to find a best fit. Fig. 1 shows the A and B absorption correction where we over-plot the uncorrected spectrum to illustrate which lines are affected. In cases where the A or B bands overlap a weak line like SiIIλ1814 the effect is considerable and measures of SiIIλ1814 should not be considered at all or with extreme care. This happens for sources J00103-0037, J03036-0023, and J20497-0554. In cases where one of the bands overlaps a stronger line like SiIII]λ1892 or AlIIIλ1860, the correction was good enough to permit accurate measures.

3.2. Redshift Estimate

Normally one uses strong narrow emission lines, preferentially from low ionization ionic species, to set the rest frame in quasars. In our case no strong narrow lines are available so we consider the peaks of Lyα, CIVλ1549 and CIII]λ1909. The Lyα peak is affected by absorption and CIVλ1549 is a HIL feature often showing blueshifts and/or asymmetries (Gaskell 1982; Espey et al. 1989; Corbin 1990; Tytler & Fan 1992; Marziani et al. 1996; Richards et al. 2002; Baskin & Laor 2005; Sulentic et al. 2007). CIII]λ1909 is blended with SiIII]λ1892 and FeIII that is especially prominent in this region and could well affect the peak wavelength of the blend. This is especially true in Pop. A sources. Pop. B sources show a rather weak Fe spectrum making the CIII]λ1909 peak a more reliable z estimator.

Another option is to use the low ionization line OIλ1304 whenever it is strong. It is unfortunately blended with low ionization SiIIH1304,1309 ($^2P_{3/2,1/2}^0 - ^2S_{1/2}$). Both OIλ1304 and SiIIH1304,1309 are broad lines; however they are of low ionization and in both Pop. A and B their peak shifts with respect to rest frame should be consistent with Hβ or FeII, and therefore be rather modest, within a few hundred km s⁻¹ (Sulentic et al. 2012; Marziani et al. 2013). There is no hint of large systematic Hβ broad component (where the broad component represents the line core and will be defined in Section 4.3) peak shifts for all Pop. A sources (the majority in our sample) and ≈ 60% of Pop. B sources (Marziani et al. 2003a).

Photoionization simulations in the (n_{H}, U) region of interest show $\text{O I}\lambda 1304 \approx 2 \text{ Si II}\lambda 1304, 1309$ and this is confirmed in the spectrum I Zw 1 where $\text{O I}\lambda 1304$ and $\text{Si II}\lambda 1304, 1309$ are resolved. The two components of the $\text{Si II}\lambda 1304, 1309$ doublet are set to the same intensity (i.e., we assume an optically thick case). We model the blend $\text{O I}\lambda 1304 + \text{Si II}\lambda 1304, 1309$ with 5 Gaussians; the three components of the O I feature are produced by Bowen fluorescence mechanism, and should show ratios consistent with their transition probabilities. Generating a model spectrum in IRAF (lines broadened to 4000 km s^{-1}) yields a rest frame peak wavelength of $1304.8 \pm 0.2 \text{ \AA}$ (in vacuum) which we use as a reference for our VLT spectra. We also used $\text{He II}\lambda 1640$ to check the restframe assignment, in the objects when it is clearly visible (J00103-0037, J00521-1108, J02287+0002, J02390-0038 and J23509-0052). Examination of Fig. 1 reveals that the peak of $\text{O I}\lambda 1304$ in source J00521-1108 is not observed clearly. We use $\text{C III}\lambda 1909$ to set the rest frame in this case. Redshifts obtained for three quasars, J01225+1339, J03036-0023 and J23509-0052, were obtained from $\text{O I}\lambda 1304$, and are consistent with the redshift obtained with $\text{C III}\lambda 1909$. There are other sources J00103-0037, J02287+0002, J02390-0038 and J20497-0554 where the redshift estimation using both $\text{O I}\lambda 1304$ and $\text{C III}\lambda 1909$ are not in good agreement (see Cols. 3 and 4 of Table 1). The largest disagreement was found for J02287+0002, with $\Delta z \approx 0.0097$. In this case, the uncertainty is so large to affect the interpretation of line profiles, and we are forced to repeat the line fitting with the assumption of two different redshifts.

Fig. 1 shows the deredshifted VLT-FORS1 spectra for our sample of 8 quasars.

4. Data Analysis

4.1. Quasar Systematics

Quasar spectra are not all alike. There are significant differences in line intensity ratios and broad line profiles from object to object (Bachev et al. 2004; Marziani et al. 2010). More importantly, these differences can be organized in a systematic way (Boroson & Green 1992). Since the early 1990s several authors have stressed the importance of the E1 of quasars (e.g., Gaskell et al. 1999). Sulentic et al. (2000; 2007) expanded the E1 trends into a 4-dimensional space involving optical, UV and X-ray measures. They also defined spectral types along a sequence occupied by AGN in an optical plane involving Fe II and FWHM $\text{H}\beta$ parameters (Sulentic et al. 2002). Objects at extreme ends of the E1 sequence are very different at almost all wavelengths and median spectra computed in spectral bins within this plane emphasize systematic changes in broad line properties (Sulentic et al. 2002, 2007). The most effective divider of the two quasar types appears to be at FWHM of the $\text{H}\beta$ broad component (BC) $\text{H}\beta_{\text{BC}} \approx 4000 \text{ km s}^{-1}$ for low-to-moderate luminosity sources (Marziani et al. 2009). The

limit on FWHM corresponds to Eddington ratio $L/L_{\text{Edd}} \sim 0.2 \pm 0.1$ (Marziani et al. 2003b).

Sulentic et al. (2002) gridded the BC of $\text{FWHM}(\text{H}\beta_{BC})$ versus $R_{\text{FeII}} = W(\text{FeII}\lambda 4570)/W(\text{H}\beta_{BC})$ parameter plane into bins of fixed $\Delta \text{FWHM} = 4000 \text{ km s}^{-1}$ and $\Delta R_{\text{FeII}} = 0.5$. Quasar spectra in different bins are different in many measures. As mentioned earlier, the largest differences are found between NLSy1-like objects, Pop. A, and broader sources of Pop. B with $\text{FWHM}(\text{H}\beta_{BC}) \gtrsim 4000 \text{ km s}^{-1}$.

Bins A1, A2, A3 are defined in terms of increasing FeII λ 4570 (see Fig. 1 of Sulentic et al. 2002). Median composite UV spectra of low- z quasars were computed by Bachev et al. (2004). However, assignment to population and spectral type was originally done on the H β spectral range that was available for every source included in the composites. In the case of high redshift quasars, the H β spectral range is customarily not available. A proper analysis of the spectrum then requires that sources are assigned to either Pop. A or B, if not to a spectral type, from UV data alone. The two following criteria comes from the analysis of optical lines profiles; previous work has shown that they can be applied to the UV lines as well.

1. Broad line width. The intermediate ionization lines AlIII λ 1860 and SiIII] λ 1892 are found to be equivalent to H β broad component, with their FWHM in close agreement (Paper II). At high luminosity the limit $\text{FWHM} = 4000 \text{ km s}^{-1}$ must be increased to consider its dependence on luminosity. Following Marziani et al. (2009), we can set $\text{FWHM} \approx \text{FWHM}_0 \left(\frac{L}{10^{45}}\right)^{\frac{1-a}{2}}$ with $\text{FWHM}_0 \approx 4000 \text{ km s}^{-1}$. The limit should be considered as indicative since the value of a is not known with a high precision. However, high luminosity sources with $\text{FWHM} \lesssim 4000 \text{ km s}^{-1}$ are found to be of Pop. A;
2. Evidence of a prominent red wing indicative of a possible very broad component (VBC); Pop. B sources show CIV λ 1549 profiles that resemble the H β ones (Marziani et al. 1996). A prominent redward asymmetry described by several authors (w.g., Wills et al. 1993; Corbin 1995; Punsly 2010; Marziani et al. 2010) is present in both CIV λ 1549 and H β . This feature, if prominent, easily and uniquely identify Pop. B sources.

Two additional discriminating UV spectral properties are the following:

1. CIV λ 1549 equivalent width. According to Bachev et al. (2004) there is a rather abrupt discontinuity in $W(\text{CIV}\lambda 1549)$ between spectral types A1 and A2, from $\approx 80 \text{ \AA}$ (A1) to $\approx 40 \text{ \AA}$ (A2). $W(\text{CIV}\lambda 1549) \lesssim 40 + 2\sigma \text{ \AA}$ is a sufficient condition to identify a Pop. A source albeit not a necessary one, since A1 sources do not satisfy this condition.

2. Prominence of AlIII λ 1860 and SiIII λ 1892 with respect to CIII λ 1909. The A3 and A4 spectral types show intensity ratios AlIII λ 1860/SiIII λ 1892 \gtrsim 0.5 and SiIII λ 1892/CIII λ 1909 \gtrsim 1.

In addition, Pop. A sources show CIV λ 1549 blueshift at half maximum intensity that are of larger amplitude than in Pop. B. However, not all Pop. A sources show blueshifts like most Pop. B sources (Sulentic et al. 2007). CIV λ 1549 blueshifts are expected to be orientation dependent if the CIV λ 1549 emitting gas is due to an outflow or wind (e.g., Flohic et al. 2012; Richards 2012, and references therein). A criterion based on CIV λ 1549 blueshift will be useful only to identify and confirm the most extreme Pop. A sources, and will not be of general validity to distinguish Pop. A and B.

Previous and current work indicates that assignment to population is relatively straightforward for most sources (Bachev et al. 2004; Marziani et al. 2010; Sulentic et al. 2013, Sulentic et al., in preparation). Some ambiguity may be present for sources right at the boundary between Pop. A and B i.e., between spectral types A1 and B1.

4.2. Methodological Considerations on Multicomponent Fits

The SPECFIT IRAF task (Kriss 1994) allows us to fit the continuum, emission and absorption line components, FeII and FeIII templates, etc. We fit the emission lines in three spectral ranges: (1) 1340-1450 Å to model the 1400Å blend most likely due to SiIV λ 1397 and OIV λ 1402 (Wills & Netzer 1979); (2) 1450–1680 Å for analysis of CIV λ 1549 and (3) 1750–2050 Å for analysis of the 1900Å blend.

4.3. Line Components

We base our SPECFIT analysis on several previous observational results described in the previous Paper I and II that point toward three different components in broad line profiles (see Marziani et al. 2010).

1. A BC showing a roughly symmetric profile with FWHM in the range 1000-5000 km s⁻¹. It is consistent with the component identified by Matsuoka et al. (2008). This BC dominates LILs in Balmer lines of Pop. A sources while it becomes less prominent in Pop. B. The most relevant one is that H β can be described by a Lorentz function in Pop. A sources (Véron-Cetty et al. 2001; Sulentic et al. 2002) and by the sum of 2

Gaussians in Pop. B sources (a BC unshifted + a broader redshifted component, the very broad component VBC (e.g., Zamfir et al. 2010).

2. A VBC, as seen in LILs and HILs of most Pop. B sources but is absent from Pop. A profiles. The VBC can be modeled as a Gaussian (FWHM $\sim 10000 \text{ km s}^{-1}$) often with a significant shift to the red. It can be called a defining property of Pop. B sources. This component is clearly identified in the $\text{CIV}\lambda 1549$ line of Pop. B objects, and is also appreciable on the red side of $\text{CIII]}\lambda 1909$ of Pop. B objects J00103-0037 and J02390-0038 that are discussed in this paper.
3. A blueshifted broad component (BLUE), defined as the residual emission in the $\text{CIV}\lambda 1549$ line after subtracting a scaled $\text{H}\beta$ profile (Marziani et al. 2010). This BLUE component is often prominent in $\text{CIV}\lambda 1549$ and $\text{Ly}\alpha$ of Pop. A sources. It is much less intense in radio-loud Pop. B sources (Marziani et al. 1996; Punsly 2010; Richards et al. 2011). We model this profile as a blueshifted Gaussian. The Gaussian approximation is probably inappropriate especially if the BLUE component is strong: this component is believed to be produced in a partially-obscured radial flow, not in a virialized emitting system.

Our multicomponent description of the broad line profile is rather crude as it involves mostly symmetric functions. While an unshifted symmetric function is expected for virial broadening, BLUE and the VBC are not necessarily Gaussian. A more accurate representation of BLUE may be obtained through a skew Gaussian. However, in the fitting of $\text{H}\beta$ for Pop. B sources, two Gaussians provide a remarkably good fit in most objects and in median composites (Zamfir et al. 2010; Marziani et al. 2013).

BLUE has been introduced because of the large blueshifted emission observed in $\text{CIV}\lambda 1549$ of A3 and A4 sources: the large $\text{CIV}\lambda 1549/\text{H}\beta$ ratio on the blue side of the line profile clearly indicates different physical conditions than in the line core. The origin of BLUE may be ascribed to a predominantly radial outflow in a radiation driven wind context (e.g. Elvis 2000). A physically motivated definition of the VBC involves the ionization stratification that is likely found in Pop. B sources (as per echo mapping studies, e.g. Peterson & Wandel 1999): since no significant VBC was detected in the FeII blends even at the highest S/N, the VBC can be properly associated with the innermost BLR part where ionization is too high to allow for significant singly-ionized iron emission. The VBC can account for the difference in full profile line width between Pop. B $\text{CIV}\lambda 1549$ and $\text{H}\beta$. At the same time, if motion is predominantly virial, the VBC gas will be responding first to continuum changes, as found in some reverberation studies (e.g. Peterson & Wandel 1999, who consider Pop. B sources). In (Paper II, Table 1) we tested that our method yields results consistent with $\text{H}\beta$ RM, and not with $\text{CIV}\lambda 1549$ RM.

We then use the results of Marziani et al. (2010) and Paper II: the BC of SiIII] λ 1892, AlIII λ 1860 and CIV λ 1549 lines is similar to the one of H β , including the FWHM and profile shape, either Gaussian or Lorentzian. The similarity helps us to define whether an object is Population A or B in this paper. We use the BC (and not the full line) intensity to compute the line ratios considered in our method (Section 7.1).

Baldwin et al. (1996) presented a similar analysis. Their Fig. 2 organizes spectra in a sequence that is roughly corresponding to E1, going from AlIII λ 1860-strong sources to objects whose spectra show prominent CIII] λ 1909 along with weak AlIII λ 1860 (Bachev et al. 2004). Two of the three line components they isolated correspond to the ones we consider in this paper: a blue-shifted feature, and a more symmetric, unshifted and relatively narrow component that we call LIL-BC. Less obvious is the correspondence of a third feature, although it appears to be the redshifted part of what we call the VBC.

4.4. FeII and FeIII Emission

FeII emission is not strong in the spectral range we studied. Significant FeIII emission is however expected close to and underlying the 1900Å blend, especially for Population A sources (Francis et al. 1991; Vanden Berk et al. 2001). Our approach is completely empirical and employs an FeII + FeIII template taken from templates successfully used in Paper I (Sec. 3.2 provides more details) and Paper II. We adopt an FeII template based on a CLOUDY simulation and is not very far from the preferred model of Brühweiler & Verner (2008), and the FeIII template of Vestergaard & Wilkes (2001). The FeII intensity scale of the template is anchored to the FeII UV 191 multiplet intensity, although we repeat that FeII is in general weak. This allows to reliably constrain FeII emission underlying CIV λ 1549 and the 1900Å blend. Similarly the FeIII intensity is set by a feature external to the 1900Å blend (2080Å).

4.5. Expected emission from the three components

We looked for evidence of three possible components as described above: BC and BLUE component for Pop. A and BC, BLUE, VBC for Pop. B sources. The three components show different strength in different lines, and are negligible in some lines, simplifying the interpretation of blended features.

4.5.1. Pop. A

The $\text{CIV}\lambda 1549$ and $\text{HeII}\lambda 1640$ are modeled assuming that a BC and a BLUE component is present in both lines. The BC and BLUE component of $\text{HeII}\lambda 1640$ account for the flat shape of broad $\text{HeII}\lambda 1640$ emission on the red side of $\text{CIV}\lambda 1549$.

The 1400\AA blend is modeled assuming a single BC and a BLUE component similar to the ones of $\text{CIV}\lambda 1549$. Since $\text{OIV]}\lambda 1402$ and $\text{SiIV}\lambda 1397$ are inextricably blended together, we consider the total blend flux for metallicity analysis (Section 6.3). However, high-density gas should emit negligible intercombination $\text{OIV]}\lambda 1402$. In the extreme Pop. A sources the BC could be ascribed to mainly $\text{SiIV}\lambda 1397$, while the BLUE component only is a blend of both $\text{SiIV}\lambda 1397$ and $\text{OIV]}\lambda 1402$. In those cases the $\text{SiIV}\lambda 1397 + \text{OIV]}\lambda 1402$ blend closely resembles the shape of $\text{CIV}\lambda 1549$.

We expect that the $\text{AlIII}\lambda 1860$ doublet is emitted exclusively in the BC, the region where FeII is also emitted. This is empirically confirmed by the aspect of the 1900\AA blend in many sources, where we do not see any evidence of BLUE nor VBC in $\text{AlIII}\lambda 1860$. We remark that the $\text{AlIII}\lambda 1860$ doublet is relatively unblended, and that a BLUE feature as strong as in the $\text{CIV}\lambda 1549$ profile of Pop. A sources would not easily escape visual detection. The same is also true for $\text{SiIII]}\lambda 1892$. Several fits that included a BLUE component in $\text{CIII]}\lambda 1909$ yielded 0 intensity, implying a large $\text{CIV}\lambda 1549/\text{CIII]}\lambda 1909$ (Marziani et al. 2010).

The BLUE component is very weak or undetectable in the vast majority of the $\text{H}\beta$ profiles analyzed in Marziani et al. 2003a (but see Zamfir et al. 2010 for several cases of $\text{H}\beta$ BLUE), while prominent in $\text{Ly}\alpha$; the $\text{Ly}\alpha/\text{H}\beta$ ratio in this component is high. In summary, the BLUE component is visually strong in $\text{Ly}\alpha$ and $\text{CIV}\lambda 1549$. A $\text{HeII}\lambda 1640$ BLUE component is needed for a self-consistent fit of the $\text{CIV}\lambda 1549+\text{HeII}\lambda 1640$ blend.

Since the shift and FWHM are assumed the same for all lines (and templates) in the 1900\AA blend, the only free parameters in addition to shift and FWHM are the intensities of 6 components: two from the templates, $\text{SiII}\lambda 1814$ and $\text{AlIII}\lambda 1860$ that are not heavily blended, and $\text{SiIII]}\lambda 1892$ and $\text{CIII]}\lambda 1909$. The SPECFIT analysis is especially helpful to measure in a non-subjective way, taking all constraints into account, the two parameters that are most affected by blending: the intensity of $\text{SiIII]}\lambda 1892$ and $\text{CIII]}\lambda 1909$ (any $\text{FeII}\lambda 1914$ contribution in excess to the one of the adopted template is included in the estimated $\text{CIII]}\lambda 1909$ intensity).

4.5.2. Pop. B

As pointed out by Marziani et al. (2010) the “plateau” appearance of the far red wing of $\text{CIV}\lambda 1549$ is accounted for a BLUE component and a redshifted VBC of $\text{HeII}\lambda 1640$, whose shifts and widths match the ones of $\text{CIV}\lambda 1549$.

The 1400\AA blend is fit with a single BLUE, BC and VBC. The VBC is rather faint (left panels of Figs. 2, 3 and 4) allowing for an estimate of the BC. However, considering that the blend is due to five components of $\text{OIV}\lambda 1402$ and two of $\text{SiIV}\lambda 1397$, whose relative intensities are unknown, we again consider the total blend flux for metallicity analysis (Section 6.3).

No VBC emission is observed (or expected) in $\text{AlIII}\lambda 1860$, FeIII and FeII . These constraints help also to make the fits less ambiguous. However, the presence of a VBC in $\text{CIII}\lambda 1909$ and $\text{SiIII}\lambda 1892$ complicates the fit of the 1900\AA blend. In any case, considering that we can expect the VBC to be assimilable to a shifted Gaussian with $\text{FWHM} \sim 10000\text{ km s}^{-1}$, the unblended part of the $\text{CIII}\lambda 1909$ VBC provides a strong constraint. Considering that the wavelength separation between $\text{SiIII}\lambda 1892$ and $\text{CIII}\lambda 1909$ is $\approx 3000\text{ km s}^{-1}$, $\ll \text{FWHM VBC}$, what we model is most likely blended $\text{SiIII}\lambda 1892$ and $\text{CIII}\lambda 1909$ VBC emission.

We also fit absorption lines when they were needed in the `SPECFIT` routine along with the emission line components described above. They are shown in red in the lower panels of the Figures 2 to 4. In the case of the BAL quasars, we modeled the BAL profiles using several absorption components.

4.6. Errors

Apart from the effect of noise that is treated as statistical source of error, we identify five main sources of error that may significantly affect our measures.

1. A & B atmospheric bands correction (already described in Section 3.1). The most serious effect is when the A/B band overlaps $\text{SiII}\lambda 1814$.
2. Line profile shape, Gaussian or Lorentzian (Pop. A or B). The distinction between Pop. A and B is based on line width with the boundary at $\text{FWHM H}\beta \approx 4000\text{ km s}^{-1}$ in low luminosity quasars and around $\approx 5000\text{ km s}^{-1}$ at higher luminosity such as the eight sources presented here. Most of our quasars are unambiguously Pop. A or B because of line width and because Pop. B sources show an $\text{H}\beta$ VBC, while Pop. A sources a prominent $\text{CIV}\lambda 1549$ BLUE component. In these cases only one

profile shape (Gaussian or Lorentzian) was fitted. A posteriori, we can say that the estimated line ratios are rather insensitive to the emission component profile shape: assuming a Gaussian or Lorentzian profile yields the same ratio for the strongest lines (i.e., C_{IV}λ1549, Si_{III}]λ1892, Al_{III}λ1860) upon which our analysis is based (with an uncertainty of ~10%).

3. Rest-frame determination using O_Iλ1304 or C_{III}]λ1909. In some cases the redshift estimates derived from the two lines do not agree, most likely because of absorptions present in O_Iλ1304 and because this is not a very intense line. The principal impact of uncertainty in the rest frame placement is estimation of the peak wavelength of C_{IV}λ1549. If the line peak differs from 1549Å, the BC intensity is diminished and we infer a greater contribution from the BLUE component. Similarly, for the blend 1900Å, the rest frame shift may increase or decrease our estimate for the strength of C_{III}]λ1909 with consequent decrease or increase of the Si_{III}]λ1892 contribution. This additional source of uncertainty affects J02287+0002, J02390-0038 and J20497-0554. However, only in the case of J02287+0002 the redshift difference produces a significant effect due to a $\Delta z \approx 0.0097$.
4. Fe_{II} intensity (continuum placement). Broad Fe_{II} emission can produce a pseudo-continuum affecting our estimates of emission line intensities. Si_{II}λ1814 is especially affected in our spectra because it is weak. Al_{III}λ1860 is similarly affected when it is weak. The effect is less noticeable for C_{IV}λ1549 since expected Fe_{II} emission underlying the C_{IV}λ1549 line is weak also for strong Fe_{II} emitters. The Fe_{III}(UV34) and Fe_{II} emission is not very strong and a posteriori we find that there is no significant effect with the exception of Si_{II}λ1814 measures but the uncertainty can be included in the one associated with continuum placement, that contributes to the statical error.
5. BAL quasars principally affect the blue side of C_{IV}λ1549. We also find an absorption feature between Fe_{III}λ1787 and Si_{II}λ1814 (eg. Fig. 4). In sources J01225+1339 and J02287+0002 derived line intensities should be viewed with care since we fit unabsorbed components where the total flux eaten by absorptions is unknown.

In the case of C_{III}]λ1909 we need to consider the possibility that the profile is narrower because there might be a contribution from different regions: indeed, the SPECFIT routine usually converges toward a narrower profile if the C_{III}]λ1909 width is not constrained. The effect depends on the strength of the Fe_{III} λ 1914 feature which is expected to be prominent only in extreme Pop. A sources (Paper I). These sources of uncertainty are included, when appropriate, in the errors reported in Table 2. From the above considerations it is however

clear that a faint line like $\text{SiII}\lambda 1814$ can be used mainly for confirmatory purposes because of the large errors plaguing its intensity estimates.

Finally, we note that the errors derived from the SPECFIT task are much smaller than the errors reported here. The reason is that the errors reported by the tasks are formal errors associated with the multicomponent fit only.

5. Results of Line Component Analysis on Individual Objects

In Figures from 2 to 4 we show our best fits for the VLT sample taking into account the considerations reported in Section 4. In the left panels we present the fits for the $\text{SiIV}\lambda 1397$ line, the center panels are for the $\text{CIV}\lambda 1549$ line and the right panels are for the the 1900\AA blend. The fluxes and equivalent widths are in Tables 2 and 4. Table 3 shows the weak lines around $\text{CIV}\lambda 1549$. For $\text{CIV}\lambda 1549$ and $\text{SiIV}\lambda 1397$ lines we show the BC, BLUE and the VBC. Errors are at a 2σ confidence level, and include the sources of uncertainty described in Section 4.6. Errors are then quadratically propagated according to standard practice to compute intensity ratios and their logarithm.

We present in the following a phenomenological description of the fits.

5.1. Pop. A Objects

We show the fits for our four Pop. A objects in the Figure 2.

- J02390-0038 – This object is borderline since $\text{FWHM(BC)} \sim 4600 \text{ km s}^{-1}$ places it close to the boundary between Pop. A and Pop. B, at high L . In support of Pop. B assignment, we note that the $\text{CIV}\lambda 1549$ profile is best fitted assuming a VBC emitting region. Also, we find $\text{FeII}\lambda 1787$ to be weaker than $\text{SiII}\lambda 1814$. On the other hand, $\text{CIII}\lambda 1909$ is flat topped and has a very similar intensity as $\text{SiIII}\lambda 1892$ and the blend is best fitted using Lorentzian profiles. This object shows a very strong BLUE component in $\text{CIV}\lambda 1549$ that is also indicative of a Pop. A source. $\text{SiIV}\lambda 1397$ has a similar flat topped profile as in $\text{CIII}\lambda 1909$ and probably as in $\text{CIV}\lambda 1549$. We fit $\text{SiIV}\lambda 1397 + \text{OIV}\lambda 1402$ blend following the $\text{CIV}\lambda 1549$ fit. Since the strongest and less ambiguous features indicate Pop. A, we assign this object to Pop. A and use Lorentzian profiles to fit all the BCs.
- J03036-0023 – We estimate for this source a $\text{FWHM(BC)} \sim 3700 \text{ km s}^{-1}$ and we use a Lorentzian function to fit the BCs. The peak of $\text{CIV}\lambda 1549$ is blueshifted and requires

a strong BLUE component. The bump on the red side of $\text{CIV}\lambda 1549$ can be accounted for by $\text{HeII}\lambda 1640$ BC and BLUE components. There is no evidence for a red shifted component in $\text{CIII}\lambda 1909$. $\text{AlIII}\lambda 1860$ is prominent. Unfortunately the blue wing of $\text{SiII}\lambda 1814$ and the red wing of $\text{FeII}\lambda 1787$ are affected by A band absorption.

- J20497-0554 – This source shows $\text{FWHM(BC)} \sim 3800 \text{ km s}^{-1}$. As for J03036-0023, the $\text{CIV}\lambda 1549$ line can be accounted for by an unshifted BC (assumed Lorentzian) and a considerable contribution of a BLUE component. We see a prominent $\text{AlIII}\lambda 1860$ line and $\text{FeII}\lambda 1787$. $\text{SiII}\lambda 1892$ is affected by several narrow absorption lines; however, it is obviously strong. The lack of a red wing on $\text{CIII}\lambda 1909$ suggests that no VBC is present. There are several absorption lines in the wings of $\text{SiIV}\lambda 1397$. However, the line profile can be extrapolated over them.
- J23509-0052 – This source has $\text{FWHM(BC)} \sim 3600 \text{ km s}^{-1}$. $\text{CIV}\lambda 1549$ shows a slight blue asymmetry with a BLUE component required to model it. The contribution of FeII is small and $\text{FeII}\lambda 1787$ is weak. $\text{CIII}\lambda 1909$ is very strong. $\text{AlIII}\lambda 1860$ is affected by A band absorption; the profile we fit is probably an upper limit. This object could well belong to spectral type A1 that includes Pop. A sources with the lowest $R_{\text{FeII}} (\lesssim 0.5)$. Five absorption lines affect the $\text{SiIV}\lambda 1397 + \text{OIV}\lambda 1402$ blend; luckily, they do not affect the core of the blend.

5.2. Pop. B Objects

- J00103-0037 – This source has a $\text{FWHM(BC)} \sim 4500 \text{ km s}^{-1}$. The red side of $\text{CIV}\lambda 1549$ is blended with $\text{HeII}\lambda 1640$. Fitting a BC with no shift plus a BLUE component to $\text{CIV}\lambda 1549$ leaves a very large residual on the red side. A redshifted VBC is needed to model the spectrum (Fig.3 upper center). The faint narrow line under $\text{CIV}\lambda 1549$ can be explained as the narrow component (NC) of $\text{CIV}\lambda 1549$ (see Sulentic et al. 2007). The presence of a similar NC in $\text{CIII}\lambda 1909$ could possible explain the large residual seen $\sim 1900\text{\AA}$. We specifically note the prominent $\text{CIII}\lambda 1909$ emission and weak (but detected) $\text{AlIII}\lambda 1860$ (Fig. 3 upper right). The FeII “bump” at 1787\AA (UV 191) is appreciable. Fainter FeII emission is relatively unimportant because FeII creates a pseudo-continuum. $\text{SiII}\lambda 1814$ is compromised by A-band absorption. The blend at 1900\AA includes a $\text{CIII}\lambda 1909$ VBC and the fit indicates $\text{CIV}\lambda 1549 / \text{CIII}\lambda 1909$ (VBC) ≈ 7 which is reasonable. We found several absorption lines on the blue side of the

$\text{SiIV}\lambda 1397 + \text{OIV}] \lambda 1402$ blend (Fig. 3 upper left), significantly affecting its BLUE component that seems at any rate to be fainter than the one of $\text{CIV}\lambda 1549$.

- J00521-1108 – This source shows the noisiest spectrum in the sample. We fit a $\text{FWHM(BC)} \sim 5300 \text{ km s}^{-1}$ with $\text{CIV}\lambda 1549$ requiring a large VBC to account for the red wing. (Fig. 3 lower center). Absorption features seriously affect the $\text{CIV}\lambda 1549$ profile. The profile of $\text{CIII}] \lambda 1909$ is strongly asymmetric due to some sort of absorption on the red side. $\text{AlIII}\lambda 1860$ is weak and consistent with pop. B (Fig. 3 lower right). We decide not to carry out a fit of the $\text{SiIV}\lambda 1397 + \text{OIV}] \lambda 1402$ blend because it is too noisy.

5.3. BAL QSOs

We fit our two BAL quasars using Lorentzian profiles following Sulentic et al. (2006a). We remind that the identification of $\text{CIII}] \lambda 1909$ in the BAL quasars and in sources with strong $\text{AlIII}\lambda 1860$ is debatable (Hartig & Baldwin 1986): strong $\text{FeII}\lambda 1914$ could take the place of most $\text{CIII}] \lambda 1909$ emission.

- J01225+1339 – $\text{CIV}\lambda 1549$ is highly affected by two broad absorption lines (Fig. 4 upper center) with blueshifts of 5200 and 10800 km s^{-1} at peak absorption with equivalent widths/ $\text{FWHM} -12\text{\AA} / 3900 \text{ km s}^{-1}$ and $-25\text{\AA} / 5200 \text{ km s}^{-1}$, respectively. The blueshift of the $\text{CIV}\lambda 1549$ peak leads us to suspect a large BLUE emission component. The 1900\AA blend shows absorptions coincident with $\text{FeII}\lambda 1787$ and the blue side of $\text{SiII}\lambda 1814$ which is however unambiguously detected (Fig. 4 upper right). $\text{AlIII}\lambda 1860$ is prominent which implies that this a Pop. A source. The $\text{FWHM(BC)} \sim 4400 \text{ km s}^{-1}$ is consistent with a high-luminosity Pop. A source. It is also possible that this BAL quasar is an outlier like Mark 231 at low- z (Sulentic et al. 2006b), in other words an extreme Pop. A object. The $\text{CIII}] \lambda 1909$ is well fitted with a Lorentzian profile. Broad A band atmospheric absorption lies over $\text{SiIII}] \lambda 1892$. The 1400\AA blend is also affected by two broad absorption line on both sides of the line (Fig. 4 upper left). As in previous cases, we made a fit following the $\text{CIV}\lambda 1549$ fit.
- J02287+0002 – This object has a very complex spectrum. On the one hand, it has a $\text{FWHM(BC)} \approx 4700 \text{ km s}^{-1}$. Considering that the FWHM limit between Pop. A and B is increasing with luminosity, the FWHM(BC) is within the limit of Pop. A but close to the boundary with Pop. B. The lines profiles are better fit with Lorentzians. On the other hand, however, it shows features that are typical of extreme Pop. A sources: prominent $\text{FeII}\lambda 1787$, strong $\text{AlIII}\lambda 1860$, no $\text{CIII}] \lambda 1909$ VBC (Fig. 4 middle right).

The CIII]λ1909 line is not very flat topped but the similar intensities of CIII]λ1909 and SiIII]λ1892 remind the case of J02390-0038. We assign J02287+0002 to Pop. A also because it has a strong blue-shifted component in CIVλ1549 atypical to Pop. B objects (Fig. 4 middle center). The CIVλ1549 BAL shows a blueshift of 9100 km s⁻¹ at deepest absorption, a EW of -14 Å and a FWHM of 4600 km s⁻¹. As in the case of J01225+1339, the SiIVλ1397 + OIV]λ1402 blend profile is severely affected by two broad absorption lines on both sides (Fig. 4 middle left).

The estimated rest frame of this quasar differs by ~ 1300 km s⁻¹ using OIλ1304 and CIII]λ1909. This is the largest discrepancy in our sample. In order to evaluate the effect of the z discrepancy we performed two fits using both rest frames. The middle panels of Figure 4 use the OIλ1304 restframe. In the 1900Å blend, we found a contribution of SiIII]λ1892 similar to CIII]λ1909. If we use the CIII]λ1909 inferred rest frame that we show in the lower panels of Figure 4, CIII]λ1909 becomes stronger with a resultant decrease of SiIII]λ1892. A similar effect occurs for CIVλ1549 broad and blue-shifted components.

Summing up, we are able to assign a Pop. A/B identification to all sources in our sample. The two BAL quasars appear as objects of extreme Pop. A; for J02287+0002 the assignment depends on the assumed redshift. However, the most likely estimate is based on the OIλ1304 line and is $z \approx 2.726$, and implies Pop. A features. Fig. 4 stands as a neat example of the importance of accurate redshift determination for quasars, as the interpretation of the source spectrum can be made different by a $\Delta z \approx 0.0097$.

6. Diagnostics of Ionizing Photon Flux

The physical conditions of photoionized gas can be described by electron density n_e , hydrogen column density N_c , metallicity (Z ; normalized to solar), shape of the ionizing continuum, and the ionization parameter U . The latter represents the dimensionless ratio of the number of ionizing photons and the electron density n_e or, equivalently, the total number density of hydrogen n_H , ionized and neutral.¹ Both U and n_H are related through the equation

$$U = \frac{\int_{\nu_0}^{+\infty} \frac{L_\nu}{h\nu} d\nu}{4\pi n_H c r^2} = \frac{Q(H)}{4\pi n_H c r^2} \quad (1)$$

¹In a fully ionized medium $n_e \approx 1.2 n_H$. We prefer to adopt the definition based on n_H because it is the one employed in the CLOUDY computations.

where L_ν is the specific luminosity per unit frequency, h is the Planck constant, ν_0 the Rydberg frequency, c the speed of light, and r can be interpreted as the distance between the central source of ionizing radiation and the line emitting region. $Q(H)$ is the number of H-ionizing photons. Note that $n_{\text{H}}U$ is, apart from the constant c , the ionizing photon flux

$$c n_{\text{H}}U = \Phi(H) = \frac{Q(H)}{4\pi r^2}. \quad (2)$$

If we know *the product of* n_{H} and U , we can estimate the radius r of the BLR from Eq. 1:

$$r_{\text{BLR},\Phi} = \sqrt{\frac{Q(H)}{4\pi c(n_{\text{H}}U)}}. \quad (3)$$

$r_{\text{BLR},\Phi}$ is the “photoionization” r_{BLR} as defined in Paper I. The dependence of U on r_{BLR} was used by Padovani & Rafanelli (1988) to derive central black hole masses assuming a plausible average value of the product $n_{\text{H}}U$. The typical value of n_{e} was derived at that time from semiforbidden line CIII] λ 1909 which implied that the density could not be much higher than $n_{\text{e}} \approx 10^{9.5} \text{ cm}^{-3}$ (Osterbrock & Ferland 2006). Padovani & Rafanelli (1988) derived an average value $\langle U \cdot n_{\text{e}} \rangle \approx 10^{9.8}$ from several sources where r_{BLR} had been determined from reverberation mapping, and for which the number of ionizing photons could be measured from multiwavelength observations. The average value was then used to compute black hole masses for a much larger sample of Seyfert 1 galaxies and low- z quasars (Padovani & Rafanelli 1988; Padovani et al. 1990). Wandel et al. (1999) compared the results of the photoionization method with the ones obtained through reverberation mapping, found a very good correlation for the masses computed with the two methods, and concluded that “both methods measure the mass of the central black hole.” A similar method based on the H β luminosity was proposed by Dibai (1984), who retrieved the ionizing luminosity from the luminosity of H β . Bochkarev & Gaskell (2009) verified that Dibai mass estimates agree with reverberation-mapping mass estimates.

In Paper II we showed that the ionizing photon flux estimated from UV lines is also in close agreement with reverberation mapping BLR distance from continuum source. Photoionization methods can at least provide an alternative method to deduce r_{BLR} with an accuracy comparable to reverberation mapping. The approach of this paper follows from the results of Paper II, in which intermediate and high-ionization lines are used as a diagnostic of the ionizing photon flux. There are three main issues that are of relevance for a general population of quasars: (1) the actual physical conditions within the BLR, and specifically (2) the contribution of relatively low density gas ($n_{\text{H}} \sim 10^{10} \text{ cm}^{-3}$). A third special issue is the estimate of the quasar metallicity since previous studies agree on super solar metallicity for high z quasars (e.g. Hamann & Ferland 1993; Ferland et al. 1996; Nagao et al. 2006; Simon & Hamann 2010).

6.1. Physical Conditions in the Emitting Regions

The method used to estimate the physical conditions of the emitting region is described in Paper I. Here we summarize the basic aspects as well as the complications arising from dealing with sources that are different from extreme sources Pop. A. To this aim, we apply and further develop the empirical technique that has been discussed in Paper II.

We base our interpretation of line ratios on a multidimensional grid of CLOUDY (Ferland et al. 1998, 2013) simulations, (see also Korista et al. 1997) to derive U and n_{H} from our spectral measurements. Simulations span the density range $7.00 \leq \log n_{\text{H}} \leq 14.00$, and $-4.50 \leq \log U \leq 00.00$, in intervals of 0.25. Each simulation was computed for a fixed ionization parameter and density assuming plane parallel geometry. The 2D grid of simulations was repeated twice assuming $N_{\text{c}} = 10^{23}$ and 10^{24} cm^{-2} . Several cases were computed also for $N_{\text{c}} = 10^{25} \text{ cm}^{-2}$. Metallicity was assumed to be either solar or five times solar. Two alternative input continua were used: 1) the standard AGN continuum of CLOUDY which is equivalent to the continuum described by Mathews & Ferland (1987) and 2) the low- z quasar continuum of Laor et al. (1997b). Computed line ratios are almost identical for fixed (U, n_{H}) . For this paper we use the (U, n_{H}) maps computed for the Laor et al. (1997b) continuum (Figure 5 of Paper I). It is the ionizing luminosity that differs by more than a factor of 2 for a fixed specific continuum luminosity (as considered in Section 8) since the same U is reached at smaller distance for the continuum with fewer ionizing photons. This is taken into account when estimating r_{BLR} (Section 8).

Feldman et al. (1992) give a critical density value for $\text{SiIII}] \lambda 1892$ $n_e \sim 2 \cdot 10^{11} \text{ cm}^{-3}$. $\text{AlIII} \lambda 1860$ is a permitted transition with large transition probability ($A \sim 5 \cdot 10^8 \text{ s}^{-1}$) and has very high and ill-defined critical density (i.e., its equivalent width goes to zero toward thermodynamic equilibrium, which occurs at very high density, when all emergent line emission is zeroed by equilibrium between collisional excitation and deexcitation). Our 2D array of CLOUDY simulations shows that the ratio $\text{AlIII} \lambda 1860 / \text{SiIII}] \lambda 1892$ is well suited to sample the density range $10^{10} - 10^{12.5} \text{ cm}^{-3}$. Within this range the $\text{SiIII}] \lambda 1892$ intensity decreases smoothly by a factor 10; above the upper limit in density, the predicted intensity of $\text{SiIII}] \lambda 1892$ decreases (Paper I). The ratio $\text{AlIII} \lambda 1860 / \text{SiIII}] \lambda 1892$ alone is, generally speaking, insufficient to constrain n_{H} . A second diagnostic ratio is needed to constrain U and to unambiguously derive n_{H} . We consider $\text{CIV} \lambda 1549 / \text{SiIII}] \lambda 1892$ and $\text{SiIV} \lambda 1397 + \text{OIV}] \lambda 1402 / \text{SiIII}] \lambda 1892$ as two diagnostic ratios suitable for constraining U .

6.2. The Contribution of Lower Density Gas

The presence of significant CIII] λ 1909 emission complicates the analysis. As pointed out, the photoionization solution for the BC suggests very high density, and in this region no CIII] λ 1909 emission is expected. The ratio AlIII] λ 1860/ SiIII] λ 1892 is diagnosing high density gas, while the CIII] λ 1909/ SiIII] λ 1892 ratio covers the domain of $n_{\text{H}} \sim 10^{10} \text{cm}^{-3}$. The spatially unresolved line emission is probably a mixture of gas in different density ionization condition, possibly following a smooth gradient. The much lower CIII] λ 1909 critical density implies that the CIII] λ 1909 line should be formed farther out than SiIII] λ 1892 and AlIII] λ 1860 if all these lines are produced under similar ionization conditions.

For the BAL quasars in our sample and AlIII] λ 1860-strong sources most of what we ascribe to CIII] λ 1909 could be actually FeIII], as suggested by Hartig & Baldwin (1986). For Pop. A sources of spectral types A3, A4, as well as for BAL quasars belonging to these A spectral types, where CIII] λ 1909 is weak with respect to SiIII] λ 1892, any contribution due to lower density gas could be neglected.

Among Pop. A2 and some A3 objects it is not so obvious that the profile of CIII] λ 1909 and SiIII] λ 1892 is the same. It could be well that the CIII] λ 1909 profile is narrower than the ones of SiIII] λ 1892 and AlIII] λ 1860 (as found for SDSS J12014+0116, see Paper I), justifying the idea of CIII] λ 1909 emission from a disjoint region or perhaps from the lower-density tail of comet-shaped clouds (Maiolino et al. 2010). Reverberation mapping studies of the 1900Å blend are scant, but they indicate that time delays in CIII] λ 1909 are a factor 2–3 larger than in CIV] λ 1549 (Onken & Peterson 2002; Metzroth et al. 2006).

Whenever strong CIII] λ 1909 is observed, as in the case of spectral type A1 and A2 and even more of Pop. B, we could reverse the question: how much does any CIII] λ 1909 emitting gas contribute to the lines used for diagnostic ratios? Negligible contribution is expected to AlIII] λ 1860. However, this is not true for CIV] λ 1549 and SiIII] λ 1892. A realistic estimate of the low density contribution to CIV] λ 1549 and SiIII] λ 1892 flux will depend on the assumptions concerning ionization and density gradient, and will be therefore model dependent.

In Paper II we showed that diagnostic ratios involving CIII] λ 1909 are not representative of H β emitting gas that is responding to continuum variations. Diagnostic ratios with CIII] λ 1909 will be avoided. Here we will follow the same approach applying an empirical correction dependent on the ratio AlIII] λ 1860/CIII] λ 1909. Generally speaking the $n_{\text{H}}U$ value derived from the ratios AlIII] λ 1860/SiIII] λ 1892 and SiIII] λ 1892/CIV] λ 1549 is associated to a single point in the parameter plane (n_{H}, U). This corresponds to a well defined solution that is biased toward high density (and therefore low r_{BLR}). As a consequence, the BLR

physical conditions cannot be described by a single value of density and ionization parameter. Even the time lag from reverberation should be interpreted with some care, since it is a single number that is a rather abstract representation of the BLR distance from the central continuum source and may not have a well-defined structural counterpart (Devereux 2013). Nonetheless, a correction based on the $\text{AlIII}\lambda 1860/\text{CIII}\lambda 1909$ ratio can lower the product $n_{\text{H}}U$ increasing the derived r_{BLR} and minimize the bias in the photoionization estimates with respect to reverberation lag (i.e. the product of the speed of light times the time lag, $c\tau$), as shown in Paper II. We apply the following correction to the derived r_{BLR} :

$$\log r_{\text{BLR},\phi} - \log c\tau \approx 0.69 \log W(\text{AlIII}\lambda 1860)/W(\text{CIII}\lambda 1909) + 0.49 \quad (4)$$

This is the same correlation found by Paper II updated including an improved $c\tau$ value (Negrete et al. 2013).

6.3. Metallicity

In high z quasars, the strength of $\text{NV}\lambda 1240$ relative to $\text{CIV}\lambda 1549$ and $\text{HeII}\lambda 1640$ suggests supersolar chemical abundances (Hamann & Ferland 1993, 1999). Chemical abundances may be well 5 to 10 times solar (Dhanda et al. 2007), with $Z \approx 5Z_{\odot}$ reputed typical of high z quasars (Ferland et al. 1996). The E1 sequence seems to be mainly a sequence of ionization in the sense of a steady decrease in prominence of the low-ionization BC toward Population B (Marziani et al. 2001, 2010). However, this is not to neglect that metal-enrichment also plays a role, especially for the most extreme Pop. A sources i.e., those in bin A3 and higher (Sulentic et al. 2001, 2013).

The lines employed in the present study come from carbon, silicon and aluminium; all these element can be significantly depleted from gas if dust grains are formed (e.g., Mathis 1990). However, the emitting regions where our lines are produced are thought too hot to contain significant amount of dust (a definition of BLR is right the central engine region below the dust sublimation region: e.g., Elitzur 2009). In addition Si and Al are expected to be produced under similar circumstances in the late stage of evolution of massive stars (Clayton 1983, Ch. 7). We considered three metallicity cases (1) solar; (2) constant solar abundance ratio Al:Si:C with $Z = 5Z_{\odot}$ (5Z); (3) an overabundance of Si and Al with respect to carbon by a factor 3, again with $Z = 5Z_{\odot}$ (5ZSiAl) following Paper I. This condition comes from the yields listed by Woosley & Weaver (1995) from type II Supernovae, and is meant to represent extreme cases associated with a circumnuclear burst of star formation significantly affecting the BLR gas chemical composition (e.g., Sani et al. 2010, and Paper I).

Two additional arrays of simulations as a function of ionization parameter and density were computed assuming the metallicity conditions (2) and (3) listed in the previous paragraph. If solar metallicity is simply scaled by a factor ($5Z$), the ratio $\text{AlIII}\lambda 1860/\text{SiIII}\lambda 1892$ is not strongly dependent on Z since it increases by about 40% passing from $Z = 1Z_\odot$ to $Z = 5Z_\odot$, for $\log n_{\text{H}} \approx 12$ and $\log U \approx -2$. The same is true for the $\text{SiII}\lambda 1814/\text{SiIII}\lambda 1892$ and $\text{SiIV}\lambda 1397+\text{OIV}\lambda 1402/\text{SiIII}\lambda 1892$ ratios, and for the ratios involving $\text{CIV}\lambda 1549$ in case $5Z$ (and it should be even more so if a metallicity increase is $1 \lesssim Z/Z_\odot \lesssim 5$). Therefore, we do not expect that the ratios employed are sensitive to Z ; this is a major advantage of the method and will be verified a posteriori (Section 7.2). To gain some information on Z , we consider the ratio $\text{SiIV}\lambda 1397+\text{OIV}\lambda 1402/\text{CIV}\lambda 1549$ that has been extensively used in investigation of metallicity for low and high- z quasars (e.g., Nagao et al. 2006) and that is fairly well correlated with $\text{NV}\lambda 1240/\text{Ly}\alpha$ (Shin et al. 2013). We avoid considering the ratio involving $\text{NV}\lambda 1240$ since (1) the deblending is extremely difficult without a very careful model of $\text{Ly}\alpha$ that is customarily heavily affected by narrow absorptions; (2) using $\text{Ly}\alpha$ will restrict the redshift range for which this method can be employed with our resorting to far UV space-based observations, from a minimum $z \approx 1.4$ to $z \approx 2.0$. In addition, the goal of the present method is to estimate r_{BLR} , not Z ; we only try to analyze how Z can affect r_{BLR} .

7. Results on the $z \approx 3$ Quasars

7.1. The ionizing photon flux

To estimate $\log n_{\text{H}}U$ we use the `CLOUDY` contour plots of the ratios $\text{AlIII}\lambda 1860/\text{SiIII}\lambda 1892$, $\text{CIV}\lambda 1549/\text{SiIII}\lambda 1892$, $\text{SiIV}\lambda 1397+\text{OIV}\lambda 1402/\text{SiIII}\lambda 1892$, $\text{CIV}\lambda 1549/\text{AlIII}\lambda 1860$, $\text{AlIII}\lambda 1860/\text{SiIV}\lambda 1397+\text{OIV}\lambda 1402$ and $\text{SiIV}\lambda 1397+\text{OIV}\lambda 1402/\text{CIV}\lambda 1549$ showed in Fig. 5 of (Paper I).² The data points of our objects are in regions where the ratios are well-defined. The ratio $\text{SiIV}\lambda 1397+\text{OIV}\lambda 1402/\text{CIV}\lambda 1549$ is used only to give a hint of the metallicity (see Section 7.2). The ratios $\text{CIV}\lambda 1549/\text{SiIII}\lambda 1892$, $\text{SiIV}\lambda 1397+\text{OIV}\lambda 1402/\text{SiIII}\lambda 1892$, $\text{CIV}\lambda 1549/\text{AlIII}\lambda 1860$ and $\text{AlIII}\lambda 1860/\text{SiIV}\lambda 1397+\text{OIV}\lambda 1402$ are mainly sensitive to the ionization parameter U , while $\text{AlIII}\lambda 1860/\text{SiIII}\lambda 1892$ and $\text{CIII}\lambda 1909/\text{SiIII}\lambda 1892$ (the latter is not considered in the following as discussed in Section 6.2) are mainly sensitive to density.

The diagnostic ratios were computed from the intensity of the BC of $\text{SiIII}\lambda 1892$, $\text{AlIII}\lambda 1860$,

²Note that there are regions where the ratio values are actually undefined: close to the high U limit ($\log U \gtrsim -0.3$), ratio $\text{AlIII}\lambda 1860/\text{SiIII}\lambda 1892$ (with $n_{\text{H}} \lesssim 10^9 \text{cm}^{-3}$) should not be considered.

SiIV λ 1397 and CIV λ 1549 reported in Table 2. We display on a graph a line representing the behavior of each ratio under the assumption of solar metallicity; the ideal point where the lines representing different diagnostic ratios cross determines the values of $\log n_{\text{H}}U$. Figure 5 shows the contour plots where we can see that the diagnostic ratios (except SiIV λ 1397+OIV] λ 1402/ CIV λ 1549) converge to rather well defined values. The crossing point is very precise for the objects J00521-1108, J01225+1339, J02287+0002 (using z_{CIII}), J02390-0038, J03036-0023, J20497-0554 and J23509-0052; for the remaining objects J00103-0037 and J02287+0002 (using z_{OI}), the crossing point is slightly different.

Table 5 summarizes the $\log n_{\text{H}}$ and $\log U$ values including their uncertainty. Since U and n_{H} are not independent quantities (their correlation coefficient is found to be 0.55), we adopt the appropriate formula for the errors on the product $n_{\text{H}}U$ (following Bevington 1969). As discussed in Paper II, n_{H} and U cannot be separately estimated unless a source is of extreme Pop. A.

7.2. Effects of Metallicity

The crossing point of the ratios SiIV λ 1397+OIV] λ 1402/ SiIII] λ 1892 and SiIII] λ 1814/ SiIII] λ 1892 is in principle independent on metallicity. Therefore, any significant disagreement between this crossing point and the ratios based on CIV λ 1549 may indicate chemical composition different from the assumed solar one (Section 6.3). We note also that the CIV λ 1549/SiIII] λ 1892 and CIV λ 1549/AlIII] λ 1860 usually give results that are in perfect agreement in the plane (n_{H}, U). These findings support our assumption that, if metallicity variations are present, the relative abundance Al to Si remains constant.

We attempted to isolate a CIV λ 1549 and a SiIV λ 1397 component that corresponds to the AlIII] λ 1860 and SiIII] λ 1892 lines. A large part of the emission in these lines is due to a BLUE component that is emitted in physical and dynamical conditions different from the ones of the BC emitting gas. CIV λ 1549 shows a large blueshift and is much broader than H β , SiIII] λ 1892 and AlIII] λ 1860 (Fig. 2 of Marziani et al. 2010). In spite of this consideration, we measured the intensity of the full profile. In the case of the 1400Å blend we also considered the full intensity, regardless of the line components decomposition. The 1400Å feature is too complex, a blend for the SiIV λ 1397 and OIV] λ 1402 contribution to be reliably singled out, for the wide majority of sources that are not extreme Pop. A (Paper I). Even if two components emitted under different physical and/or dynamical conditions are responsible for the 1400Å blend, the chemical composition of both components is expected to be the same (and in this case the full CIV λ 1549 intensity was used for normalization). In addition, the 1400Å full blend intensity normalized by full CIV λ 1549 intensity has been used as a

metallicity indicator in recent works (e.g., Nagao et al. 2006; Shin et al. 2013).

Generally speaking, appreciable discrepancies in the crossing point of the $1400\text{\AA}/\text{CIV}\lambda 1549$ ratio may signal a non-solar metallicity yielding an higher and a lower $1400\text{\AA}/\text{CIV}\lambda 1549$ ratio in the case of super solar and sub solar metallicity respectively, for a given ionization and density solution. However, the $1400/\text{CIV}\lambda 1549$ ratio does not provide a good constrain of metallicity because the uncertainty bands in the (n_{H}, U) plane are very large. In the case of the BAL quasars J01225+1339, and J02287+0002 if z OI λ 1304 is assumed, this ratio gives some indication of super solar metallicity. For this reason we calculated contour plots with higher metallicity values. These new plots are shown for J01225+1339, and J02287+0002 in Fig. 6 in the case of $5Z_{\odot}$ and $5Z_{\odot}\text{SiAl}$ metallicity. The agreement in the intersection points for J01225+1339, remains well defined in the case of $Z = 5Z_{\odot}$. For J02287+0002 the agreement in the intersection point becomes better for $Z = 5Z_{\odot}\text{SiAl}$. The $Z = 5Z_{\odot}\text{SiAl}$ case yields higher U and smaller n_{H} if emission line ratios involving CIV λ 1549 are considered. This reflects the increase in abundance of Si and Al with respect to C, and the fact the SiII λ 1814, SiIII] λ 1892, AlIII λ 1860 lines are emitted at lower ionization than CIV λ 1549.

In all other cases the metallicity is not well constrained, and could be well within 1 and 5 times solar. In order to be sure however, we repeated the $n_{\text{H}}U$ derivation for all sources in the $5Z_{\odot}$ case: there is no systematic difference and the dispersion is also less than the estimated $n_{\text{H}}U$ uncertainties: $\langle n_{\text{H}}U(1Z_{\odot}) - n_{\text{H}}U(5Z_{\odot}) \rangle \approx -0.02$, with rms ≈ 0.09 . If a solar metallicity had been assumed for J02287+0002, $n_{\text{H}}U(1Z_{\odot}) - n_{\text{H}}U(5Z_{\odot}\text{SiAl}) \approx 0.16$. Significant changes are expected only in the cases there is a selective enhancement of some elements over others involved in the computation of the diagnostic intensity ratios. The average effect would be $n_{\text{H}}U(1Z_{\odot}) - n_{\text{H}}U(5Z_{\odot}\text{SiAl}) \approx 0.11$ with an rms of ≈ 0.2 . We do not report all super solar cases in Table 5 since they are believed to be not correct save for J02287+0002 and J01225+1339. Numbers in bold identify the preferred Z (n_{H}, U) solutions.

We conclude that scaling the metallicity up to $Z = 5Z_{\odot}$ from $Z = 1Z_{\odot}$ yields an effect that is well below the uncertainty associated with the method, and particularly small if the ratios AlIII λ 1860/SiIII] λ 1892, SiIV λ 1397+OIV] λ 1402/SiIII] λ 1892 and CIV λ 1549/AlIII λ 1860 are considered to compute n_{H} and U . It is significant if strong enrichment of Al and Si over C occurs, so that the efforts should be focused on the identification of such cases. These cases are however believed to be relatively rare ($\approx 10\%$ at low z), and are easily identified since they generally satisfy the condition AlIII λ 1860 \gtrsim 0.5 SiIII] λ 1892, and SiIII] λ 1892 \gtrsim CIII] λ 1909 (Marziani & Sulentic 2013).

8. Photoionization Computations of Broad Line Region Distance and Black Hole Mass.

The distance of the broad line region r_{BLR} and the black hole mass (M_{BH}) are key parameters that let us understand the dynamics of the gas in the emitting region and the quasar behavior and evolution. In this work we will use a method based on the determination of $n_{\text{H}}U$ to compute $r_{\text{BLR},\Phi}$. Eq. 3 can be rewritten as

$$r_{\text{BLR},\Phi} = \frac{1}{h^{1/2}c} (n_{\text{H}}U)^{-1/2} \left(\int_0^{\lambda_{Ly}} f_{\lambda} \lambda d\lambda \right)^{1/2} d_c \quad (5)$$

where d_c is the radial comoving distance. The integral is carried out from the Lyman limit (λ_{Ly}) to the shortest wavelengths on the *rest frame* specific flux f_{λ} . For the integral we will use two Spectral Energy Distributions (SEDs): one described by Mathews & Ferland (1987) and one by Laor et al. (1997b).

Expressing $r_{\text{BLR},\Phi}$ in units of light-days, and scaling the variables to convenient units, Eq. 5 becomes:

$$r_{\text{BLR},\Phi} \approx 93 \left[\frac{f_{\lambda_0,-15} \tilde{Q}_{H,0.01}}{(n_{\text{H}}U)_{10}} \right]^{\frac{1}{2}} \zeta(z, 0.3, 0.7) \text{ lt - day} \quad (6)$$

where $f_{\lambda_0,-15}$ is the specific rest-frame flux (measured on the spectra at $\lambda_0 = 1700\text{\AA}$) in units of $10^{-15} \text{ erg s}^{-1} \text{ cm}^{-2} \text{\AA}^{-1}$. The product $n_{\text{H}}U$ is normalized to 10^{10} cm^{-3} . $\zeta(z, 0.3, 0.7)$ is an interpolation function of d_c as a function of redshift. $\tilde{Q}_{H,0.01} = \int_0^{\lambda_{Ly}} \tilde{s}_{\lambda} \lambda d\lambda$ is normalized to $10^{-2} \text{ cm} \text{\AA}$. We use \tilde{s}_{λ} to define the SED following Mathews & Ferland (1987) and Laor et al. (1997b). \tilde{Q}_H is $0.00963 \text{ cm} \text{\AA}$ in the case the continuum of Laor et al. (1997b) is considered; $\tilde{Q}_H \approx 0.02181 \text{ cm} \text{\AA}$ for Mathews & Ferland (1987). We use their average value, since the derived U and n_{H} are not sensitive to the two different shapes to a first approximation.³ The two SEDs give a small difference in the estimated number of ionizing photons.

Knowing $r_{\text{BLR},\Phi}$ we can calculate the $M_{\text{BH},\Phi}$ assuming virial motions of the gas

$$M_{\text{BH},\Phi} = f \frac{\Delta v^2 r_{\text{BLR},\Phi}}{G} \quad (7)$$

or,

$$M_{\text{BH},\Phi} = \frac{3}{4G} f_{0.75} (FWHM)^2 r_{\text{BLR},\Phi} \quad (8)$$

³Since the Laor et al. (1997b) continuum produces a fewer ionizing photons, the same value of U is obtained at a smaller distance.

with the geometry term $f_{0.75} \approx 1.0$ (Graham et al. 2011, see also Onken et al. 2004; Woo et al. 2010). Collin et al. (2006) suggest that f is significantly different for Pop.A and B sources; we do not consider here their important result for the sake of comparison with previous work (Section 9.2).

Table 6 reports the values of the $r_{\text{BLR},\Phi}$ and the $M_{\text{BH},\Phi}$ of our 8 objects and the extreme objects in the last two rows. Column 1 identifies the quasar name; Col. 2 gives the quasar comoving distance in mega parsecs [Mpc]; Cols. 3 and 4 are the continuum specific flux value at 1350Å and 1700Å respectively, Col. 5 reports the FWHM in km s^{-1} for the BCs, Col. 6 is the Population designation. Cols. (7) and (8) report the logarithm of the r_{BLR} in cm obtained from: a) the values selected from Table 5 ($r_{\text{BLR},\Phi}$); and b) corrected by low density emission using Eq. 4. Cols. (9) and (10) list the determinations of M_{BH} in solar masses in the same order as for r_{BLR} . Finally Cols. (11) and (12) is M_{BH} computed following Vestergaard & Peterson (2006) (their Eq. 11) and Shen & Liu (2012) respectively. We will explain in Section 9 how these quantities are computed.

9. Discussion

9.1. Previous work

There have been several studies aimed at computing r_{BLR} and M_{BH} . A direct measure of r_{BLR} through reverberation mapping requires an enormous amount of observational effort and has only been applied to a relatively small number of quasars: slightly less than 60 objects with $z \lesssim 0.4$ (Kaspi et al. 2000, 2005; Peterson et al. 2004; Bentz et al. 2010, 2013)). A second way to measure r_{BLR} uses a less direct method. Kaspi et al. (2000, 2005) and Bentz et al. (2009) used reverberation mapping results to find, in an empirical way, a relation between r_{BLR} and the optical continuum luminosity at 5100Å,

$$r_{\text{BLR}} \propto L^\alpha \tag{9}$$

with $\alpha \approx 0.52$. Vestergaard & Peterson (2006) obtained a similar result for the optical continuum luminosity with an $\alpha \approx 0.50$ and for the UV continuum at 1350Å, $\alpha \approx 0.53$. These relations have been used to compute the r_{BLR} not only for nearby objects, but also for high redshift, high luminosity objects. There are other works that use single epoch spectra and the continuum at 3000Å, obtaining an $\alpha \approx 0.47$ (McLure & Jarvis 2002).

We can rewrite Eq. 7 as

$$M_{\text{BH}} \propto f \frac{\text{FWHM}^2 L^\alpha}{G}. \tag{10}$$

$H\beta$ is a low ionization strong line whose FWHM has been widely used to determine the M_{BH} for objects mainly up to $z \lesssim 0.9$; above this limit IR spectrometers and large telescopes are needed to cover the redshifted line. For distant objects ($z \sim 2$), an alternative is to use $\text{CIV}\lambda 1549$, a high ionization line emitted in the UV. However, this line should be used with caution because the line is often blueshifted. This means that at least part of this line is likely emitted in an outflow (Netzer et al. 2007; Richards et al. 2011; Marziani & Sulentic 2012). Thus the estimation of M_{BH} using $\text{FWHM}(\text{CIV}\lambda 1549)$ tend to be systematically higher than those using $\text{FWHM}(H\beta)$ for objects of Population A (Sulentic et al. 2007).

9.2. Comparison with previous work

We compare $r_{\text{BLR},\Phi}$ obtained using our photoionization method with the ones estimated through the $r_{\text{BLR}} - L$ correlation in the upper panel of Fig. 7. Our $r_{\text{BLR},\Phi}$ agree well with the Bentz et al. (2013) relation: the average $r_{\text{BLR},\Phi} - r_{\text{BLR}}(L)$ is $\approx 0.14 \pm 0.10$ and -0.16 ± 0.13 without and with low-density correction, respectively.

Vestergaard & Peterson (2006) (VP06) used the relation $r_{\text{BLR}} \propto L^{0.53}$ to obtain the following formula that relates M_{BH} to the $\text{FWHM}(\text{CIV}\lambda 1549)$ and the continuum luminosity at 1350\AA :

$$\log M_{\text{BH}}(\text{CIV}) = 0.66 + 0.53 \log \left[\frac{\lambda L_{\lambda}(1350\text{\AA})}{10^{44} \text{ ergs s}^{-1}} \right] + 2 \log \left[\frac{\text{FWHM}(\text{CIV})}{\text{km s}^{-1}} \right] - s_f. \quad (11)$$

More recently, Shen & Liu (2012, S12) updated the $M_{\text{BH}} - \text{Luminosity}$ relation:

$$\log M_{\text{BH}}(\text{CIV}) = 7.295 + 0.471 \log \left[\frac{\lambda L_{\lambda}(1350\text{\AA})}{10^{44} \text{ ergs s}^{-1}} \right] + 0.242 \log \left[\frac{\text{FWHM}(\text{CIV})}{\text{km s}^{-1}} \right] - s_f. \quad (12)$$

The scale factor $s_f \approx -0.27$ sets the masses to the f value obtained by Graham et al. (2011). In Cols. 9 to 12 of Table 6 we show our $M_{\text{BH},\Phi}$ results with those using Equations 11 and 12. We do not apply corrections for radiation-pressure effects that are likely relevant especially for objects radiating at large Eddington ratio (Netzer 2009; Netzer & Marziani 2010). The difference between this computation and the one reported in Sulentic et al. (2007) is that in the latter work the BLUE component was not separated from the BC of $\text{CIV}\lambda 1549$ just to show how larger values of $\text{FWHM}(\text{CIV}\lambda 1549)$ yielded M_{BH} much larger than the ones derived from $\text{FWHM}(H\beta)$ in Pop. A objects.

We compare the masses obtained using our photoionization method with those of VP06 and S12 in Fig. 7, middle and lower panel. We use the FWHM of the BC reported in

Col. 5 of Tab. 6 as an estimator of the virial line broadening. The photoionization masses before correction agree with the prediction of the the luminosity correlation with a systematic offset of 0.32 ± 0.10 with VP06 and 0.22 ± 0.08 with SL12. The M_{BH} values obtained after correction for low density gas are systematically lower. This happens because the correction lowers the r_{BLR} and hence the M_{BH} . The agreement after correction is very good, with $\langle \log M_{\text{BH},\Phi} - \log M_{\text{BH}}(\text{VP06}) \rangle \approx 0.12 \pm 0.14$ and $\langle \log M_{\text{BH},\Phi} - \log M_{\text{BH}}(\text{SL12}) \rangle \approx 0.02 \pm 0.07$. No significant differences occur if the z CIII] λ 1909 solution is used for J02287+0002.

Fig. 7 should be looked at with two cautions. First, the correlation is dominated by the luminosity dependence of r_{BLR} , used to compute M_{BH} in both cases. Second, the spread of M_{BH} values is small, less than one order of magnitude (and most objects have indistinguishable masses within the errors). Our estimated error bars are however smaller compared to the spread expected on the basis of the $r_{\text{BLR}}-L$ correlation which is ≈ 0.33 for VP06 and ≈ 0.28 for S12 at 1σ confidence level. The two shaded bands of Fig. 7 limit the region where we can expect to find data points on the basis of the $r_{\text{BLR}}-L$ correlation.

The present results indicate that the photoionization relations can be extended and used for high redshift objects (or at least until $z \sim 3$). In order to do this, we need:

- Spectra with S/N high enough to see the profile shape that allows decomposition of the CIV λ 1549 line, especially to separate the BLUE component from the BC;
- to follow the methodological considerations explained in Section 4 .

10. Conclusions

In this paper we presented new observations of eight high redshift quasars. The spectra were meant to provide high S/N, moderate resolution data on which the SiIV λ 1397, CIV λ 1549, SiIII] λ 1892 and AlIII λ 1860 emission line profiles could be accurately analyzed. Line profile fits permitted us to isolate a specific component whose intensity ratios were used to derive values of the ionizing photon flux.

These results allowed us to compute the product $n_{\text{H}}U$ and hence the size of the BLR and the central black hole mass. The method described in this paper rests on the assumption of photoionization as the mechanism of gas heating, on the assumption of isotropic luminosity, and on line ratios predicted by CLOUDY simulations.

We found that the M_{BH} derived from the computed r_{BLR} and from the virial assumption are in good agreement with the ones derived from the luminosity-size relation. The photoionization method explored in this paper offers an estimate of r_{BLR} for each quasar, with some

advantages on the r_{BLR} valued derived from the luminosity-size correlation. The luminosity correlation suffers from large scatter and is simply extrapolated to very high luminosity without any support since there are, unfortunately, no conclusive results on reverberation of high luminosity quasars even if heroic efforts are underway (e.g. Trevese et al. 2007; Kaspi et al. 2007; Botti et al. 2010).

We repeat that our M_{BH} and r_{BLR} results are based on the product $n_{\text{H}}U$ and not on values of n_{H} and of U taken separately. To apply the photoionization method in the most effective way, determining $n_{\text{H}}U$ with the lowest uncertainty, spectral data should be of moderate resolution ($\lambda/\Delta\lambda \sim 1000$) as well as of high S/N. If the SiII λ 1814 line can be measured in an accurate way, it would be possible to derive reliable estimates of Z/Z_{\odot} . Instead, we used SiIV λ 1397+OIV λ 1402/CIV λ 1549 to constrain metallicity. Only for extreme Pop. A sources, when SiIII λ 1892 \gtrsim CIII λ 1909, it is possible to estimate the n_{H} , U and metallicity with very high S/N spectra.

The present exploratory analysis emphasized several sources of uncertainty. However, the parameter needed for r_{BLR} and M_{BH} computation, the product $n_{\text{H}}U$, seems to be fairly stable and well-defined. Even with an error of a 0.3 in logarithm, the square root will be subject to a 0.15 uncertainty in logarithm, much lower than the uncertainty associated with the r_{BLR} – luminosity correlation. The large intrinsic spread of the correlation at low luminosity, its uncertain extrapolation at very high luminosity make preferable a one-by-one determination based on physical properties of the emitting regions.

A. Negrete and D. Dultzin acknowledge support form grants IN111610-3 and IN107313 PAPIIT, DGAPA UNAM.

REFERENCES

- Appenzeller, I., et al. 1998, *The Messenger*, 94, 1
- Bachev, R., Marziani, P., Sulentic, J. W., Zamanov, R., Calvani, M., & Dultzin-Hacyan, D. 2004, *ApJ*, 617, 171
- Baldwin, J. A., Ferland, G. J., Korista, K. T., Hamann, F., & LaCluyzé, A. 2004, *ApJ*, 615, 610
- Baldwin, J. A., et al. 1996, *ApJ*, 461, 664
- Baskin, A., & Laor, A. 2005, *MNRAS*, 356, 1029

- Becker, R. H., White, R. L., & Helfand, D. J. 1995, *ApJ*, 450, 559
- Bentz, M. C., Peterson, B. M., Pogge, R. W., & Vestergaard, M. 2009, *ApJL*, 694, L166
- Bentz, M. C., et al. 2010, *ApJ*, 716, 993
- . 2013, *ApJ*, 767, 149
- Bevington, P. R. 1969, *Data reduction and error analysis for the physical sciences*
- Bochkarev, N. G., & Gaskell, C. M. 2009, *Astronomy Letters*, 35, 287
- Boroson, T. A., & Green, R. F. 1992, *ApJS*, 80, 109
- Botti, I., Lira, P., Netzer, H., & Kaspi, S. 2010, in *IAU Symposium*, Vol. 267, IAU Symposium, 198–198
- Brühweiler, F., & Verner, E. 2008, *ApJ*, 675, 83
- Clayton, D. D. 1983, *Principles of stellar evolution and nucleosynthesis*
- Collin, S., Kawaguchi, T., Peterson, B. M., & Vestergaard, M. 2006, *A&Ap*, 456, 75
- Collin-Souffrin, S., & Dumont, A. M. 1990, *A&Ap*, 229, 292
- Collin-Souffrin, S., Dyson, J. E., McDowell, J. C., & Perry, J. J. 1988, *MNRAS*, 232, 539
- Corbin, M. R. 1990, *ApJ*, 357, 346
- . 1995, *ApJ*, 447, 496
- Davidson, K., & Netzer, H. 1979, *Reviews of Modern Physics*, 51, 715
- Devereux, N. 2013, *ApJ*, 764, 79
- Dhanda, N., Baldwin, J. A., Bentz, M. C., & Osmer, P. S. 2007, *ApJ*, 658, 804
- Dibai, E. A. 1984, *Soviet Ast.*, 28, 245
- Dumont, A.-M., Collin-Souffrin, S., & Nazarova, L. 1998, *A&A*, 331, 11
- Dumont, A. M., & Mathez, G. 1981, *A&A*, 102, 1
- Elitzur, M. 2009, in *Astronomical Society of the Pacific Conference Series*, Vol. 402, *Approaching Micro-Arcsecond Resolution with VSOP-2: Astrophysics and Technologies*, ed. Y. Hagiwara, E. Fomalont, M. Tsuboi, & M. Yasuhiro, 419

- Elvis, M. 2000, *ApJ*, 545, 63
- Elvis, M., et al. 1994, *ApJS*, 95, 1
- Eracleous, M., & Halpern, J. P. 2003, *ApJ*, 599, 886
- Espey, B. R., Carswell, R. F., Bailey, J. A., Smith, M. G., & Ward, M. J. 1989, *ApJ*, 342, 666
- Feldman, U., Mandelbaum, P., Seely, J. F., Doschek, G. A., & Gursky, H. 1992, *ApJS*, 81, 387
- Ferland, G. J., Baldwin, J. A., Korista, K. T., Hamann, F., Carswell, R. F., Phillips, M., Wilkes, B., & Williams, R. E. 1996, *ApJ*, 461, 683
- Ferland, G. J., Korista, K. T., Verner, D. A., Ferguson, J. W., Kingdon, J. B., & Verner, E. M. 1998, *PASP*, 110, 761
- Ferland, G. J., et al. 2013, *Rev. Mexicana Astron. Astrofis.*, 49, 137
- Flohic, H. M. L. G., Eracleous, M., & Bogdanović, T. 2012, *ApJ*, 753, 133
- Francis, P. J., Hewett, P. C., Foltz, C. B., Chaffee, F. H., Weymann, R. J., & Morris, S. L. 1991, *ApJ*, 373, 465
- Gaskell, C. M. 1982, *ApJ*, 263, 79
- Gaskell, C. M., Brandt, W. N., Dietrich, M., Dultzin-Hacyan, D., & Eracleous, M., eds. 1999, *Astronomical Society of the Pacific Conference Series*, Vol. 175, *Structure and Kinematics of Quasar Broad Line Regions*
- Graham, A. W., Onken, C. A., Athanassoula, E., & Combes, F. 2011, *MNRAS*, 412, 2211
- Hamann, F., & Ferland, G. 1993, *ApJ*, 418, 11
- . 1999, *ARA&A*, 37, 487
- Hartig, G. F., & Baldwin, J. A. 1986, *ApJ*, 302, 64
- Hu, C., Wang, J.-M., Ho, L. C., Chen, Y.-M., Bian, W.-H., & Xue, S.-J. 2008, *ApJL*, 683, L115
- Joly, M. 1987, *A&A*, 184, 33

- Kaspi, S., Brandt, W. N., Maoz, D., Netzer, H., Schneider, D. P., & Shemmer, O. 2007, *ApJ*, 659, 997
- Kaspi, S., Maoz, D., Netzer, H., Peterson, B. M., Vestergaard, M., & Jannuzi, B. T. 2005, *ApJ*, 629, 61
- Kaspi, S., Smith, P. S., Netzer, H., Maoz, D., Jannuzi, B. T., & Giveon, U. 2000, *ApJ*, 533, 631
- Korista, K., Baldwin, J., Ferland, G., & Verner, D. 1997, *ApJS*, 108, 401
- Kriss, G. 1994, *Astronomical Data Analysis Software and Systems III*, A.S.P. Conference Series, 61, 437
- Laor, A., Fiore, F., Elvis, M., Wilkes, B. J., & McDowell, J. C. 1997a, *ApJ*, 477, 93
- Laor, A., Jannuzi, B. T., Green, R. F., & Boroson, T. A. 1997b, *ApJ*, 489, 656
- Maiolino, R., et al. 2010, *A&A*, 517, A47+
- Marziani, P., & Sulentic, J. W. 2012, *New A Rev.*, 56, 49
- . 2013, *ArXiv e-prints*
- Marziani, P., Sulentic, J. W., Dultzin-Hacyan, D., Calvani, M., & Moles, M. 1996, *ApJS*, 104, 37
- Marziani, P., Sulentic, J. W., Negrete, C. A., Dultzin, D., Zamfir, S., & Bachev, R. 2010, *MNRAS*, 409, 1033
- Marziani, P., Sulentic, J. W., Plauchu-Frayn, I., & del Olmo, A. 2013, *ApJ*, 764, 150
- Marziani, P., Sulentic, J. W., Plauchu-Frayn, I., & del Olmo, A. 2013, *A&A*, 555, A89
- Marziani, P., Sulentic, J. W., Stirpe, G. M., Zamfir, S., & Calvani, M. 2009, *A&Ap*, 495, 83
- Marziani, P., Sulentic, J. W., Zamanov, R., Calvani, M., Dultzin-Hacyan, D., Bachev, R., & Zwitter, T. 2003a, *ApJS*, 145, 199
- Marziani, P., Sulentic, J. W., Zwitter, T., Dultzin-Hacyan, D., & Calvani, M. 2001, *ApJ*, 558, 553
- Marziani, P., Zamanov, R. K., Sulentic, J. W., & Calvani, M. 2003b, *MNRAS*, 345, 1133
- Mathews, W. G., & Ferland, G. J. 1987, *ApJ*, 323, 456

- Mathis, J. S. 1990, *ARA&A*, 28, 37
- Matsuoka, Y., Kawara, K., & Oyabu, S. 2008, *ApJ*, 673, 62
- Metzroth, K. G., Onken, C. A., & Peterson, B. M. 2006, *ApJ*, 647, 901
- Nagao, T., Marconi, A., & Maiolino, R. 2006, *A&Ap*, 447, 157
- Negrete, C. A., Dultzin, D., Marziani, P., & Sulentic, J. W. 2012, *ApJ*, 757, 62
- . 2013, *ApJ*, 771, 31
- Negrete, C. A., Dultzin, D., Marziani, P., & Sulentic, J. W. 2013, *AdvSpR*, in press
- Netzer, H. 2009, *ApJ*, 695, 793
- Netzer, H., Lira, P., Trakhtenbrot, B., Shemmer, O., & Cury, I. 2007, *ApJ*, 671, 1256
- Netzer, H., & Marziani, P. 2010, *ApJ*, 724, 318
- Onken, C. A., Ferrarese, L., Merritt, D., Peterson, B. M., Pogge, R. W., Vestergaard, M., & Wandel, A. 2004, *ApJ*, 615, 645
- Onken, C. A., & Peterson, B. M. 2002, *ApJ*, 572, 746
- Osterbrock, D. E., & Ferland, G. J. 2006, *Astrophysics of gaseous nebulae and active galactic nuclei* (University Science Books)
- Padovani, P., Burg, R., & Edelson, R. A. 1990, *ApJ*, 353, 438
- Padovani, P., & Rafanelli, P. 1988, *A&A*, 205, 53
- Peterson, B. M., & Wandel, A. 1999, *ApJ*, 521, L95
- Peterson, B. M., et al. 2004, *ApJ*, 613, 682
- Punsly, B. 2010, *ApJ*, 713, 232
- Richards, G. T. 2012, in *Astronomical Society of the Pacific Conference Series*, Vol. 460, *AGN Winds in Charleston*, ed. G. Chartas, F. Hamann, & K. M. Leighly, 67
- Richards, G. T., Vanden Berk, D. E., Reichard, T. A., Hall, P. B., Schneider, D. P., SubbaRao, M., Thakar, A. R., & York, D. G. 2002, *AJ*, 124, 1
- Richards, G. T., et al. 2006, *ApJS*, 166, 470

- Richards, G. T., et al. 2011, *AJ*, 141, 167
- Sani, E., Lutz, D., Risaliti, G., Netzer, H., Gallo, L. C., Trakhtenbrot, B., Sturm, E., & Boller, T. 2010, *MNRAS*, 403, 1246
- Shen, Y., & Liu, X. 2012, *ApJ*, 753, 125
- Shin, J., Woo, J.-H., Nagao, T., & Kim, S. C. 2013, *ApJ*, 763, 58
- Simon, L. E., & Hamann, F. 2010, *MNRAS*, 407, 1826
- Sulentic, J. W., Bachev, R., Marziani, P., Negrete, C. A., & Dultzin, D. 2007, *ApJ*, 666, 757
- Sulentic, J. W., del Olmo, A., & Marziani, P. 2013, ArXiv e-prints
- Sulentic, J. W., Dultzin-Hacyan, D., Marziani, P., Bongardo, C., Braitto, V., Calvani, M., & Zamanov, R. 2006a, *Revista Mexicana de Astronomia y Astrofisica*, 42, 23
- Sulentic, J. W., Marziani, P., & Calvani, M. 2001, *X-ray Astronomy: Stellar Endpoints, AGN, and the Diffuse X-ray Background*, 599, 963
- Sulentic, J. W., Marziani, P., & Dultzin-Hacyan, D. 2000, *ARA&A*, 38, 521
- Sulentic, J. W., Marziani, P., Zamanov, R., Bachev, R., Calvani, M., & Dultzin-Hacyan, D. 2002, *ApJL*, 566, L71
- Sulentic, J. W., Marziani, P., Zamfir, S., & Meadows, Z. A. 2012, *ApJ*, 752, L7
- Sulentic, J. W., Repetto, P., Stirpe, G. M., Marziani, P., Dultzin-Hacyan, D., & Calvani, M. 2006b, *A&Ap*, 456, 929
- Trevese, D., Paris, D., Stirpe, G. M., Vagnetti, F., & Zitelli, V. 2007, *A&A*, 470, 491
- Tytler, D., & Fan, X.-M. 1992, *ApJS*, 79, 1
- Vanden Berk, D. E., et al. 2001, *AJ*, 122, 549
- Véron-Cetty, M.-P., Véron, P., & Gonçalves, A. C. 2001, *AAp*, 372, 730
- Vestergaard, M., & Peterson, B. M. 2006, *ApJ*, 641, 689
- Vestergaard, M., & Wilkes, B. J. 2001, *ApJS*, 134, 1
- Wandel, A., Peterson, B. M., & Malkan, M. A. 1999, *ApJ*, 526, 579
- Wang, H., Wang, T., Zhou, H., Liu, B., Wang, J., Yuan, W., & Dong, X. 2011, *ApJ*, 738, 85

Wills, B. J., Brotherton, M. S., Fang, D., Steidel, C. C., & Sargent, W. L. W. 1993, *ApJ*, 415, 563

Wills, D., & Netzer, H. 1979, *ApJ*, 233, 1

Woo, J.-H., et al. 2010, *ApJ*, 716, 269

Woosley, S. E., & Weaver, T. A. 1995, *ApJS*, 101, 181

Zamfir, S., Sulentic, J. W., Marziani, P., & Dultzin, D. 2010, *MNRAS*, 403, 1759

Table 1. Basic Properties of Sources and Log of Observations.

Object name (1)	m_B (2)	z (3)	Δ_z (4)	Line (5)	M_B (6)	Flux 6cm (mJy) (7)	Date (8)	DIT (9)	N_{exp} (10)	Airmass (11)	S/N (12)
J00103-0037	18.39	3.1546	0.0052	1	-25.68	0.402	2006-11-08	1139	3	1.13	60
J00521-1108	18.70	3.2364	0.0018	2	-25.39	0.432	2007-01-01	1199	3	1.22	41
J01225+1339	18.24	3.0511	0.0011	1	-25.80	*	2006-11-08	1259	2	1.34	92
J02287+0002	18.20	2.7282	0.0097	1	-25.72	0.351	2006-12-16	1259	2	1.11	67
J02390-0038	18.68	3.0675	0.0083	1	-25.36	0.429	2006-11-07	1199	3	1.47	57
J03036-0023	17.65	3.2319	0.0016	1	-26.44	0.339	2006-12-16	1259	2	1.13	88
J20497-0554	18.29	3.1979	0.0068	1	-25.79	*	2006-11-04	1259	2	1.61	54
J23509-0052	18.67	3.0305	0.0041	1	-25.36	0.411	2006-11-07	1199	3	1.12	62

*Not in FIRST

Table 2. Line Fluxes ^a

Object	CII] λ 1909		SiII] λ 1892	AlII] λ 1860	SiII] λ 1814	CIV] λ 1549			SiIV] λ 1397+OIV] λ 1402		
	BC	VBC				BC	BLUE	VBC	BC	BLUE	VBC
J00103-0037	5.0 \pm 2.1	1.2 \pm 1.4 *	2.9 \pm 1.0	2.0 \pm 0.8	1.1 \pm 0.8 :	14.3 \pm 8.3	6.3 \pm 1.8	8.7 \pm 2.4	4.3 \pm 2.4	0.8 \pm 1.5	0.5 \pm 0.9
J00521-1108	3.1 \pm 0.4	0.0 \pm 0.1 *	2.8 \pm 0.7	1.6 \pm 0.9	1.1 \pm 0.9	10.9 \pm 2.4	1.4 \pm 1.3	8.3 \pm 2.6
J01225+1339	10.7 \pm 1.4	...	8.3 \pm 1.3	4.4 \pm 2.1	1.0 \pm 1.0	22.7 \pm 6.0	14.2 \pm 1.5	...	11.2 \pm 2.9	6.7 \pm 1.9	...
J02287+0002 ⁽¹⁾	6.5 \pm 2.0	...	6.0 \pm 2.2	2.5 \pm 1.1	0.6 \pm 0.7	9.9 \pm 3.6	7.9 \pm 2.7	...	7.2 \pm 3.4	2.1 \pm 1.3	...
J02287+0002 ⁽²⁾	7.7 \pm 2.0	...	4.2 \pm 2.2	1.6 \pm 1.1	0.9 \pm 0.7	17.4 \pm 11.2	2.1 \pm 2.7	...	7.5 \pm 3.4	0.7 \pm 1.3	...
J02390-0038	4.8 \pm 1.3	0.6 \pm 1.0 *	4.7 \pm 1.2	2.2 \pm 0.6	0.8 \pm 0.7	9.8 \pm 2.4	7.6 \pm 1.2	2.0 \pm 1.3	3.2 \pm 0.7	1.8 \pm 0.8	0.2 \pm 0.3
J03036-0023	13.2 \pm 1.1	...	11.8 \pm 1.2	5.2 \pm 1.5	1.5 \pm 1.2 :	29.5 \pm 3.5	20.6 \pm 3.3	...	11.1 \pm 1.9	7.4 \pm 2.4	...
J20497-0554	8.0 \pm 1.1	...	7.4 \pm 0.6	3.0 \pm 1.3	1.5 \pm 1.5 :	18.4 \pm 2.2	9.2 \pm 2.2	...	6.6 \pm 2.5	2.0 \pm 1.1	...
J23509-0052	5.2 \pm 1.2	...	4.6 \pm 1.6	1.5 \pm 0.5	0.4 \pm 0.4	9.2 \pm 1.2	7.8 \pm 2.4	...	3.6 \pm 1.5	2.9 \pm 1.3	...

Note. — (a) Units are 10^{-14} ergs s⁻¹ cm⁻² Å⁻¹. (1) Considering z_{OI} . (2) Considering $z_{CIII}]$. (: SiII] λ 1814 approximated values due the line is affected by telluric absorptions (see Fig. 1). We do not measure SiIV] λ 1397 for J00521-1108 because they have low S/N. (*) Consistent with no emission.

Table 3. Weak lines around C $\text{IV}\lambda 1549$. ^a

Object	N $\text{IV}\lambda 1486$	Si $\text{II}\lambda 1533$	He $\text{II}\lambda 1640$	
			<i>BC</i>	<i>BLUE</i>
J00103-0037	2.4 ± 1.9	1.1 ± 0.8	1.3 ± 0.4	2.0 ± 1.8
J00521-1108	0.1 ± 0.2	1.1 ± 1.1	1.6 ± 1.2	0.1 ± 0.2
J01225+1339	...	1.0 ± 1.8	3.2 ± 3.4	4.3 ± 1.8
J02287+0002 ⁽¹⁾	0.2 ± 0.3	0.2 ± 0.2
J02287+0002 ⁽²⁾	0.6 ± 0.3	0.4 ± 0.2
J02390-0038	0.6 ± 0.7	0.3 ± 1.0	0.0 ± 0.4	1.8 ± 0.9
J03036-0023	...	1.5 ± 1.2	0.5 ± 0.5	9.2 ± 3.4
J20497-0554	0.3 ± 0.6	1.5 ± 1.5	1.8 ± 0.8	4.6 ± 2.7
J23509-0052	...	0.4 ± 0.4	0.2 ± 0.9	2.5 ± 1.6

Note. — (a) Units are 10^{-14} ergs s^{-1} cm^{-2} \AA^{-1} . (1) Considering z_{OI} . (2) Considering $z_{\text{CIII}\lambda}$. We do not show He $\text{II}\lambda 1640_{\text{VBC}}$ because is very weak, when is considered.

Table 4. Equivalent Widths.

Object	CII] λ 1909 $_{BC}$	CII] λ 1909 $_{Tot}$	SII] λ 1892	AlII] λ 1860	SII] λ 1814	CIV] λ 1549 $_{BC}$	CIV] λ 1549 $_{Tot}$	(SIV] λ 1397+OIV] λ 1402) $_{BC}$	(SIV] λ 1397+OIV] λ 1402) $_{Tot}$
J00103-0037	13.7 \pm 5.8	17.1 \pm 7.2	7.9 \pm 3.0	5.3 \pm 2.8	2.9 \pm 2.5 :	29.0 \pm 16.1	59.6 \pm 18.0	7.4 \pm 4.3	9.7 \pm 6.7
J00521-1108	8.2 \pm 1.5	8.2 \pm 2.4	7.3 \pm 2.5	4.0 \pm 2.6	2.6 \pm 2.1	21.0 \pm 12.4	40.1 \pm 14.9
J01225+1339	15.3 \pm 3.5	...	11.6 \pm 3.1	6.0 \pm 3.6	1.4 \pm 1.6	25.5 \pm 9.1	41.6 \pm 9.7	11.1 \pm 3.9	17.7 \pm 4.7
J02287+0002 ⁽¹⁾	19.3 \pm 6.7	...	17.8 \pm 5.7	7.4 \pm 3.8	1.8 \pm 2.2	26.6 \pm 6.7	48.0 \pm 20.5	18.8 \pm 6.0	24.3 \pm 6.7
J02287+0002 ⁽²⁾	22.8 \pm 6.7	...	12.3 \pm 5.7	4.7 \pm 3.8	2.6 \pm 2.2	48.2 \pm 9.6	54.0 \pm 24.6	18.8 \pm 6.0	20.7 \pm 6.7
J02390-0038	14.5 \pm 4.1	16.5 \pm 5.3	13.9 \pm 3.7	6.4 \pm 2.2	2.1 \pm 1.7	21.3 \pm 5.6	42.2 \pm 7.3	6.0 \pm 1.5	9.7 \pm 3.7
J03036-0023	12.4 \pm 1.8	...	10.9 \pm 1.8	4.6 \pm 1.6	1.3 \pm 1.1 :	19.7 \pm 3.7	33.3 \pm 4.8	6.4 \pm 1.5	10.7 \pm 2.9
J20497-0554	15.5 \pm 3.5	...	14.1 \pm 2.3	5.6 \pm 2.9	2.7 \pm 2.5 :	25.4 \pm 5.6	38.1 \pm 7.1	8.0 \pm 3.7	10.3 \pm 4.0
J23509-0052	15.8 \pm 4.0	...	13.7 \pm 5.3	4.4 \pm 1.8	1.1 \pm 0.9	22.0 \pm 4.2	40.5 \pm 10.6	7.7 \pm 3.7	14.0 \pm 5.1

Note. — (1) Considering z_{OI} . (2) Considering z_{CIII} . (: SII] λ 1814 approximated values due the line is affected by telluric absorptions.

Table 5. Hydrogen Density and Ionization Parameter.

Object	Log n_{H}			Log U			Log $n_{\text{H}}U$		
	$1Z_{\odot}$	$5Z_{\odot}$	$5Z_{\odot}$ SiAl	$1Z_{\odot}$	$5Z_{\odot}$	$5Z_{\odot}$ SiAl	$1Z_{\odot}$	$5Z_{\odot}$	$5Z_{\odot}$ SiAl
J00103-0037	12.50 ± 0.17	-2.79 ± 0.19	9.71 ± 0.22
J00521-1108	12.40 ± 0.26	-2.80 ± 0.15	9.60 ± 0.26
J01225+1339	12.43 ± 0.22	11.99 ± 0.31	11.58 ± 0.28	-2.93 ± 0.09	-2.44 ± 0.39	-2.04 ± 0.11	9.51 ± 0.21	9.55 ± 0.43	9.54 ± 0.27
J02287+0002 ⁽¹⁾	12.32 ± 0.15	11.88 ± 0.23	11.33 ± 0.38	-2.96 ± 0.24	-2.55 ± 0.40	-2.13 ± 0.22	9.36 ± 0.24	9.33 ± 0.40	9.21 ± 0.38
J02287+0002 ⁽²⁾	12.10 ± 0.32	-2.57 ± 0.28	9.53 ± 0.36
J02390-0038	12.47 ± 0.12	-3.10 ± 0.05	9.38 ± 0.11
J03036-0023	12.34 ± 0.14	-2.96 ± 0.06	9.39 ± 0.14
J20497-0554	12.28 ± 0.25	-2.93 ± 0.12	9.35 ± 0.25
J23509-0052	12.15 ± 0.24	-2.91 ± 0.09	9.24 ± 0.24

Note. — (1) Considering z_{OI} . (2) Considering $z_{\text{CIII]}}$. We show in bold numbers the ones that we consider the best.

Table 6. The Size of the Broad Line Region and the Black Hole Masses.

Object	d_C [Mpc]	$f(1700\text{\AA})^a$		$f(1350\text{\AA})^a$ [$X10^{-15}$]	FWHM_{BC} [km s^{-1}]	Pop.	$\text{Log}(r_{BLR})$ [cm]		$\text{Log}(M_{BH})$ [M_\odot] ^b			
		$X10^{-15}$	$X10^{-15}$				ϕ^*	low dens*	ϕ^*	low dens*	VP06 ^b	S12 ^c
(1)	(2)	(3)	(4)	(5)	(6)	(7)	(8)	(9)	(10)	(11)	(12)	
J00103-0037	6510	4.8 ± 1.0	6.8 ± 1.4	4500 ± 1200	B	18.10 ± 0.12	17.90 ± 0.14	9.29 ± 0.26	9.08 ± 0.27	9.11	9.17	
J00521-1108	6586	6.1 ± 1.5	8.8 ± 2.1	5300 ± 1600	B	18.21 ± 0.14	17.94 ± 0.25	9.54 ± 0.30	9.27 ± 0.36	9.32	9.24	
J01225+1339	6415	8.1 ± 1.6	10.9 ± 2.2	4400 ± 1000	A [†]	18.29 ± 0.15	18.08 ± 0.25	9.45 ± 0.25	9.24 ± 0.32	9.19	9.25	
J02287+0002 ⁽¹⁾	6091	7.4 ± 2.7	8.4 ± 3.0	3900 ± 1200	A	18.42 ± 0.21	18.22 ± 0.21	9.48 ± 0.34	9.28 ± 0.34	9.00	9.17	
J02287+0002 ⁽²⁾	6091	7.4 ± 2.7	8.4 ± 3.0	4100 ± 1200	A [†]	18.26 ± 0.20	18.19 ± 0.21	9.36 ± 0.32	9.29 ± 0.33	9.05	9.17	
J02390-0038	6448	6.9 ± 2.1	9.9 ± 3.0	4600 ± 1000	A [†]	18.34 ± 0.16	18.10 ± 0.16	9.55 ± 0.25	9.30 ± 0.25	9.21	9.24	
J03036-0023	6582	20.5 ± 5.7	30.0 ± 8.4	3700 ± 600	A	18.58 ± 0.10	18.39 ± 0.15	9.60 ± 0.17	9.40 ± 0.21	9.29	9.45	
J20497-0554	6552	6.6 ± 1.3	9.5 ± 1.9	3800 ± 600	A	18.35 ± 0.13	18.17 ± 0.22	9.39 ± 0.19	9.21 ± 0.26	9.04	9.22	
J23509-0052	6398	4.8 ± 1.0	6.1 ± 1.2	3600 ± 800	A	18.33 ± 0.19	18.22 ± 0.23	9.32 ± 0.27	9.21 ± 0.30	8.88	9.11	

Note. — (a) Units of the flux at 1350 and 1700Å are in $\text{ergs s}^{-1} \text{cm}^{-2} \text{\AA}^{-1}$. We show the comparison between our computations and those using: (b) the Vestergaard & Peterson (2006) method; and (c) the Shen & Liu (2012) work. They report an uncertainty of 0.66 and 0.54 dex at 2 sigma confidence respectively. (†) According to the FWHM it is classified as Pop. B, but has other spectral characteristics of pop. A objects. See Section 5. (*) The listed values computed assuming an average SED of Laor et al. (1997b) and Mathews & Ferland (1987) with a scatter ± 0.17 dex. We used the bold numbers of Table 5 to compute $r_{BLR,\phi}$. (1) Considering z_{OI} . (2) Considering z_{CIII}

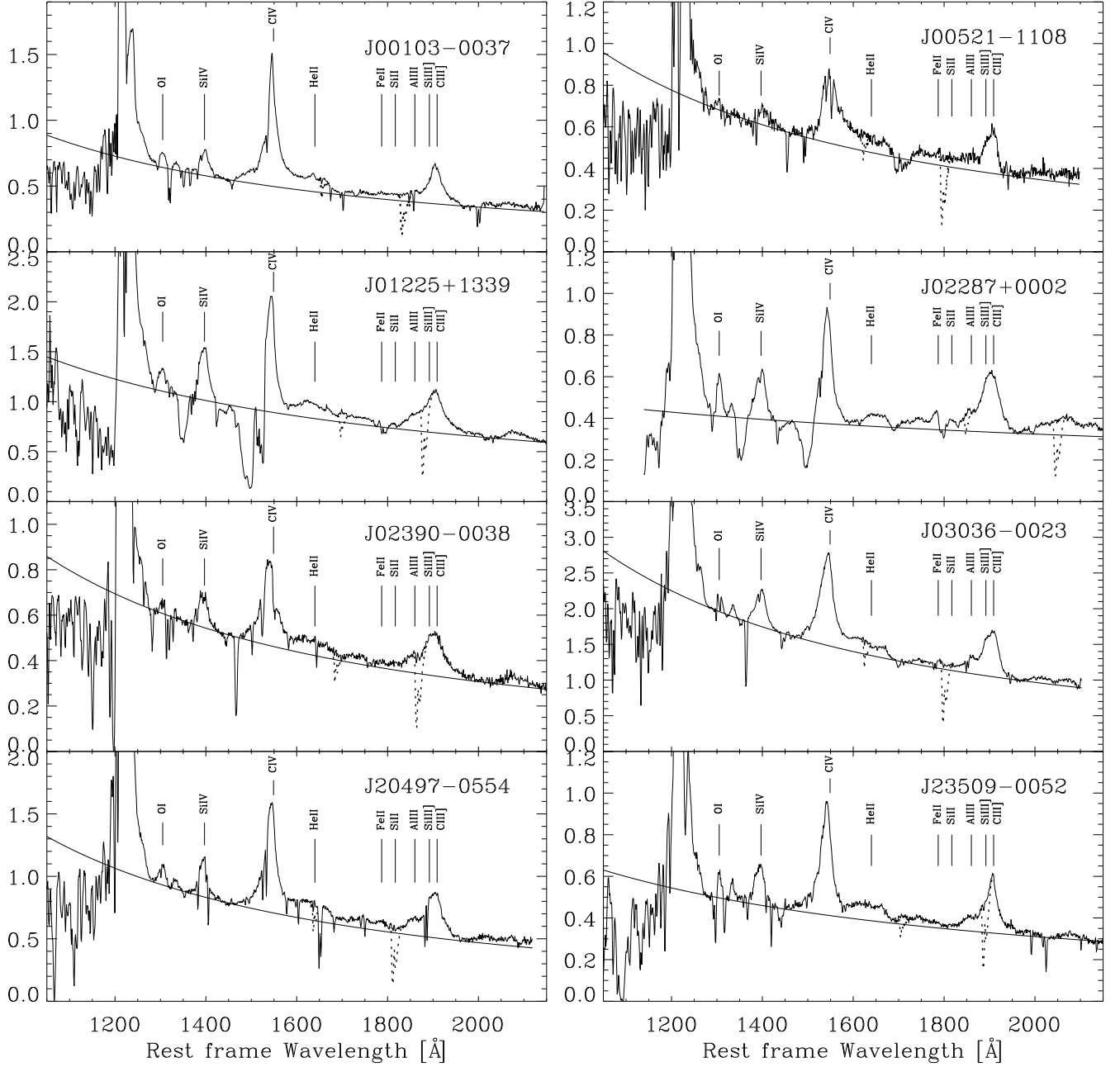


Fig. 1.— Sample of 8 VLT spectra in rest frame wavelength. Abscissa is observed wavelength in \AA , ordinate is specific flux in units $10^{-13} \text{ ergs s}^{-1} \text{ cm}^{-2} \text{ \AA}^{-1}$ corrected for Milky Way Galactic extinction. The superimposed dotted line is before atmospheric bands subtraction. We show the fitted continuum and the positions of the lines of our interest $\text{CIII}] \lambda 1909$, $\text{SiII}] \lambda 1892$, $\text{AlIII} \lambda 1860$, $\text{SiII} \lambda 1814$, $\text{FeII} \lambda 1787$, $\text{CIV} \lambda 1549$ and $\text{SiIV} \lambda 1397$. J01225+1339 and J02287 are BAL quasars.

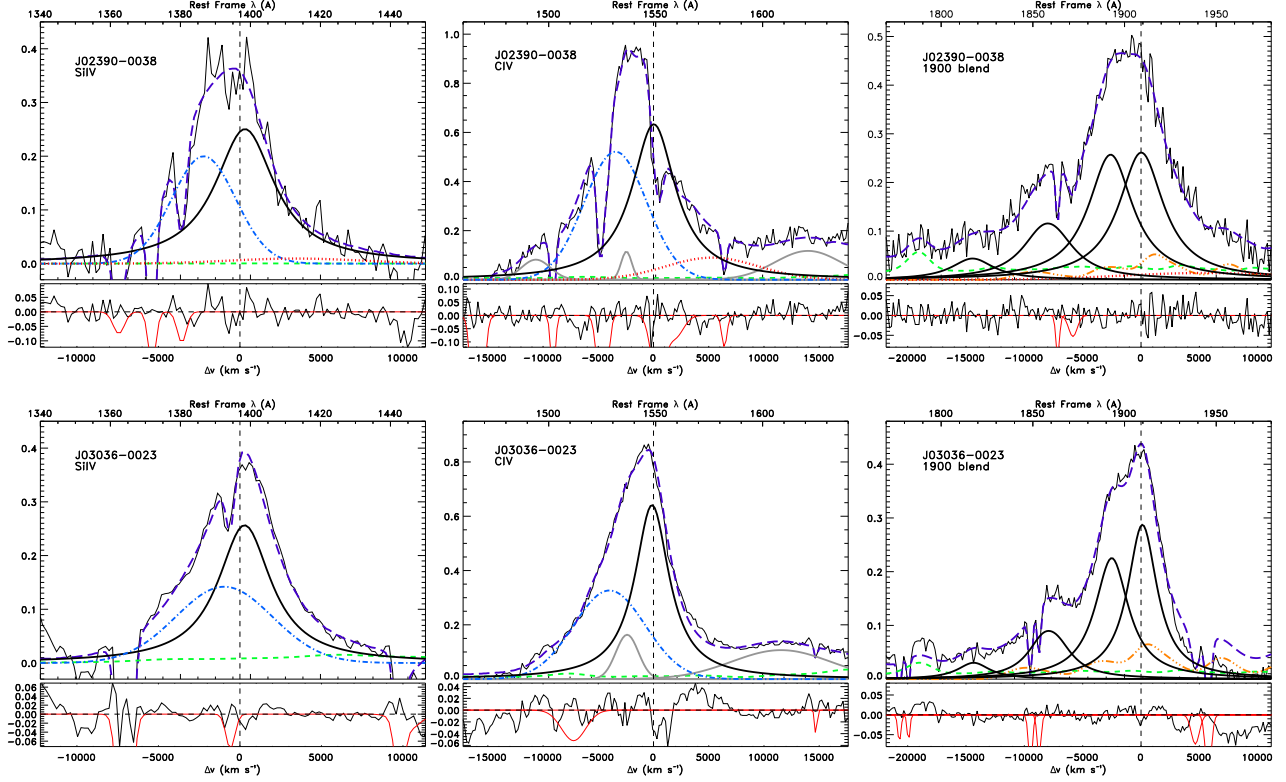


Fig. 2.— Fits for Pop. A objects: J02390-0038, J03036-0023, J20497-0554 and J23509-0052. Upper panels show the fits and the lower panels under the fits show the residuals and also the fitted absorptions lines shown in red. Upper abscissa is rest frame wavelength in Å, lower abscissa is in velocity units, ordinate is specific flux in arbitrary units. Vertical dashed line is the restframe for CIVλ1549 and CIII]λ1909. Purple long dashed line is the fit, solid black lines are the BCs: SiIVλ1397 in left panels, CIVλ1549 in center panels and CIII]λ1909, SiIII]λ1892, AlIIIλ1860, SiIIλ1814 in right panels. For AlIIIλ1860 we show the sum of the doublet. Short green dashed line is FeII. FeII is shown in orange dash-triple-dot line in the right panels. Blue dash-dot line in the left and center panels is the blue-shifted component of SiIVλ1397 and CIVλ1549 respectively. Dotted red line is the VBC, present also in CIII]λ1909 for Pop. B objects. In the center panels we show with grey lines the contribution of NIVλ1486, SiIIλ1533 and HeIIλ1640 core and blue-shifted components. For colors see online figures.

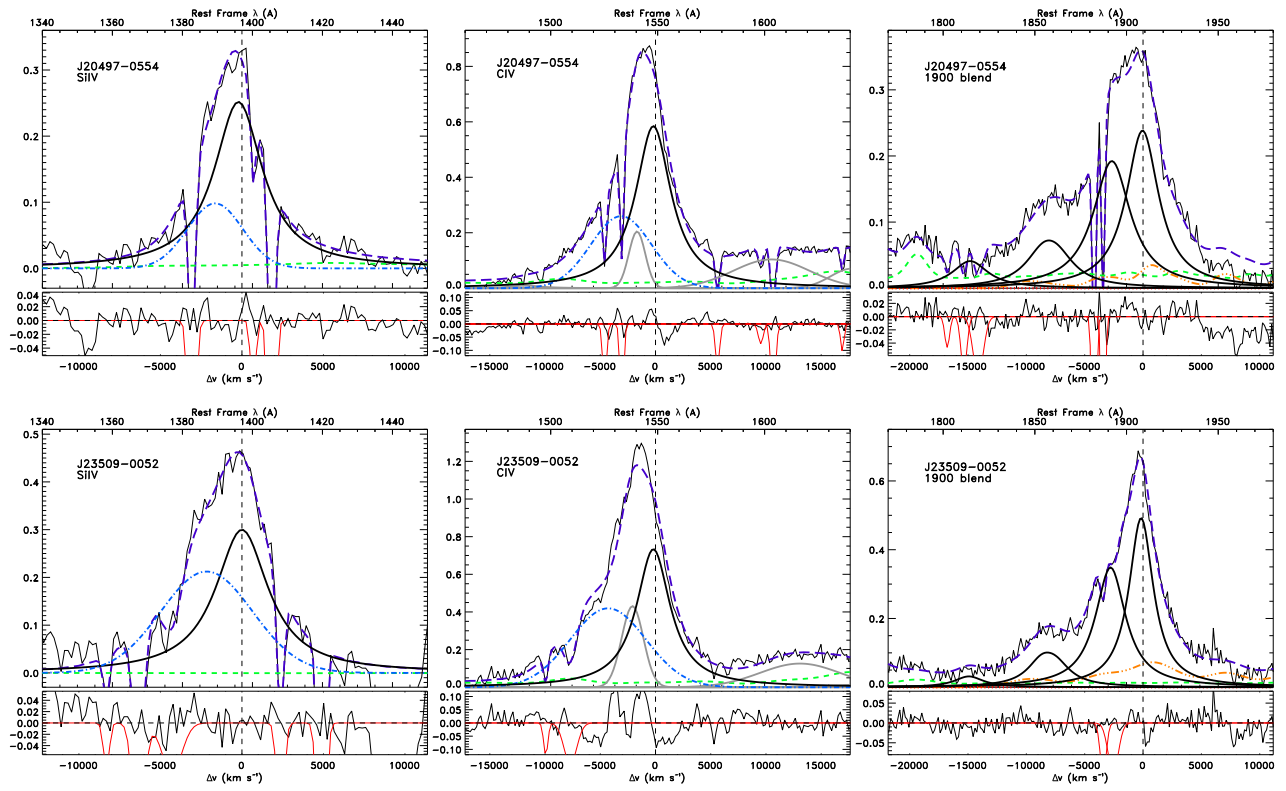


Fig. 2 – Cont.

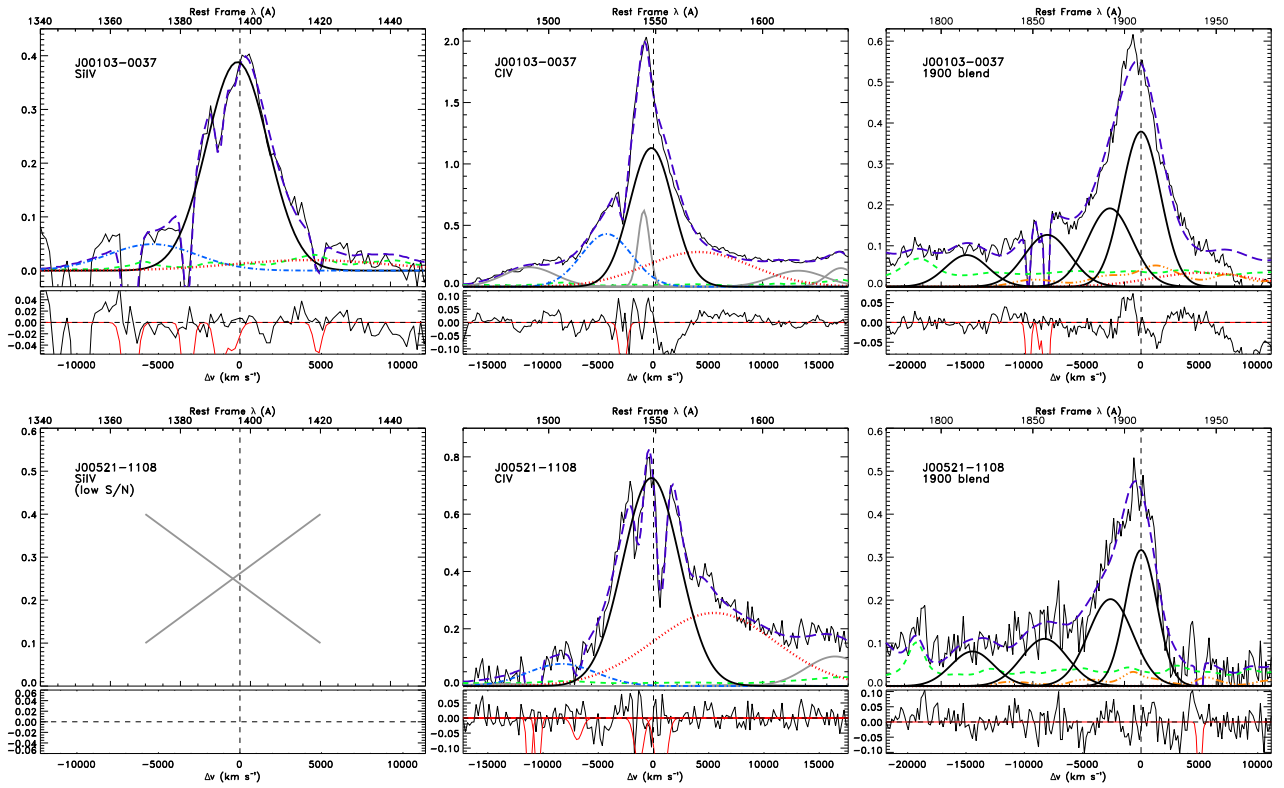


Fig. 3.— Fits for Pop. B objects: up J00103-0037 and low J00521-1108. Units and meaning of symbols are the same of Fig. 2.

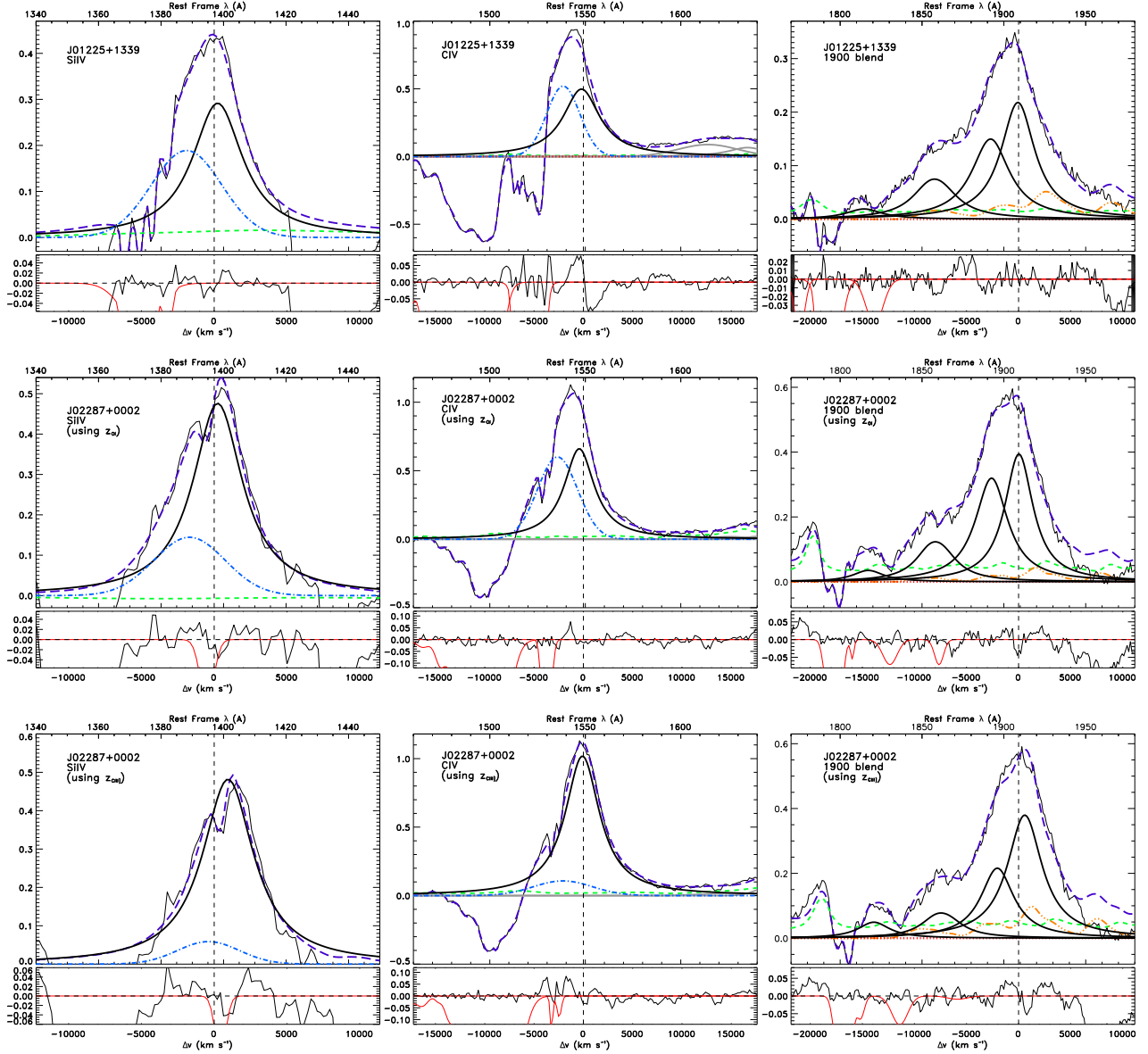


Fig. 4.— Fits for BAL quasars: up J01225+1339, middle J02287+0002 using $z_{O\text{I}\lambda 1304}$ rest frame, low J02287+0002 using $z_{C\text{III}\lambda 1909}$ rest frame. Note in J02287+0002 the line displacement with the consequently line intensity changes, specially in $C\text{III}\lambda 1909$, $\text{SiIII}\lambda 1892$ and $C\text{IV}\lambda 1549$ broad and blue-shifted components. Units and symbols are the same as in Fig. 2.

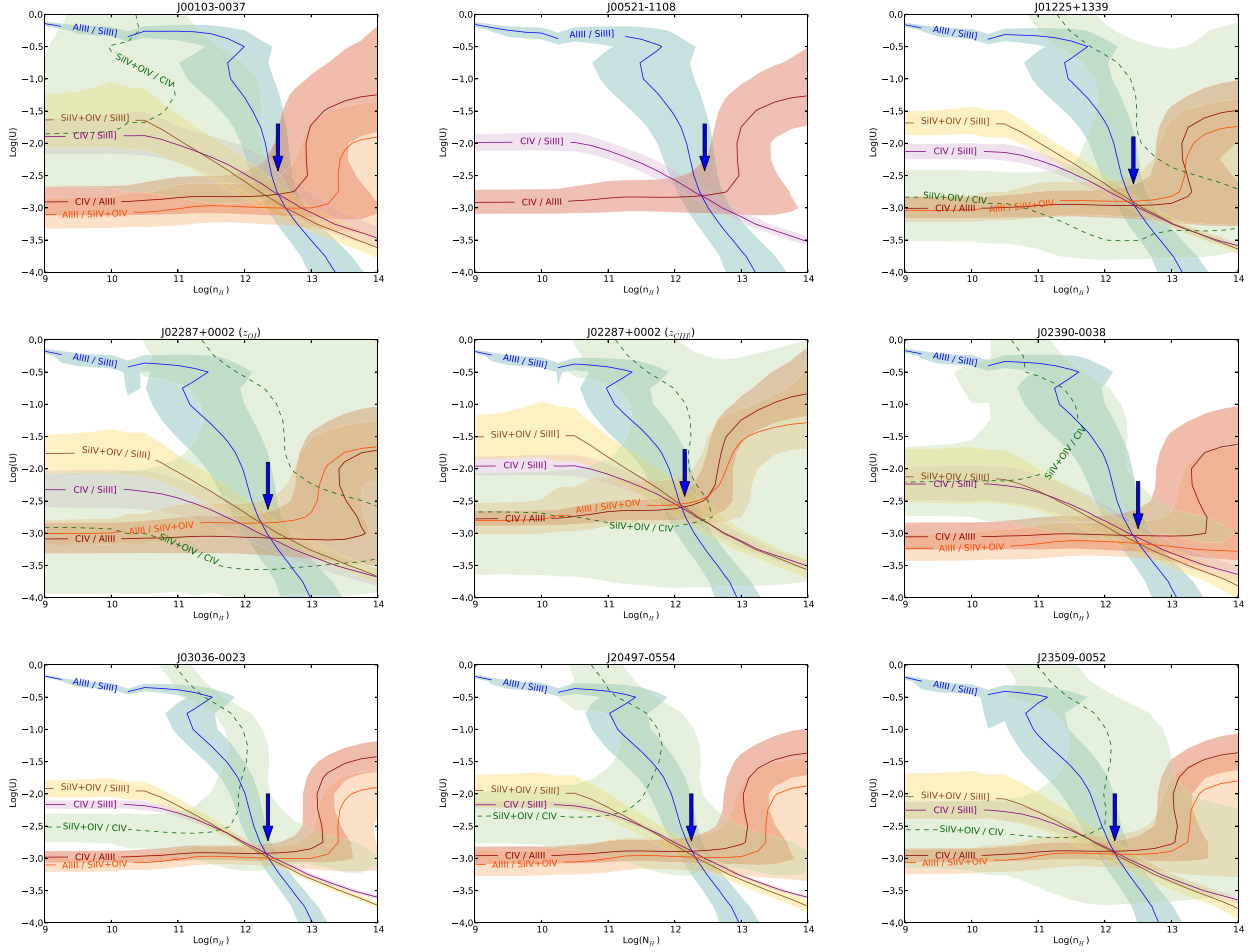


Fig. 5.— Contour plots for our sample. We show the two cases for the BAL quasar J02287+0002. Abscissa is electron density in cm^{-3} , ordinate is the ionization parameter, both in logarithm scale. The point where the isocontours cross (marked with an arrow) determines the values of $\text{Log}n_{\text{H}}$ and $\text{Log}U$. $\text{SiIV}\lambda 1397+\text{OIV}\lambda 1402/\text{CIV}\lambda 1549$ is in dashed line because we do not use it for constrain $n_{\text{H}}U$, but to determine the metallicity (see Section 6.3). The shaded area are the error bands at 2σ confidence.

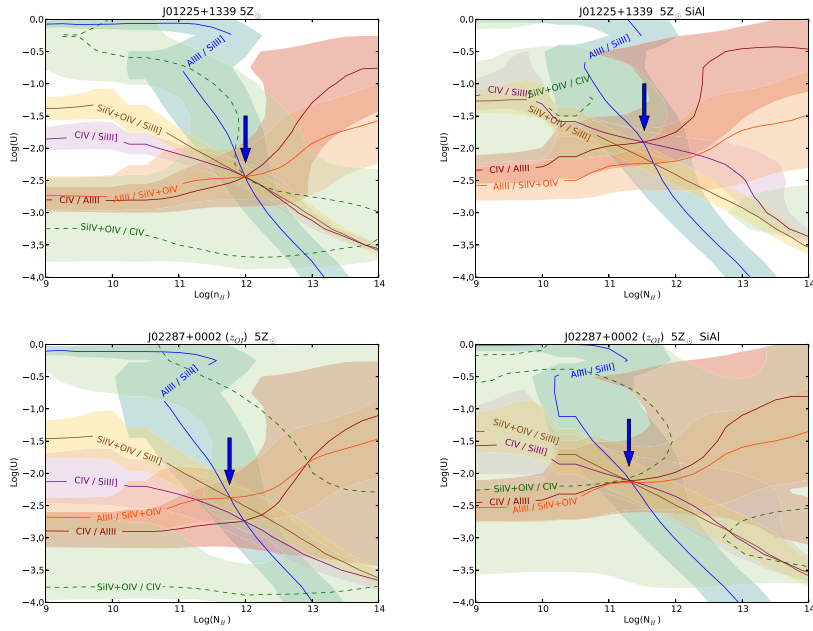


Fig. 6.— Left: Contour plots from the array of simulations computed for $Z = 5Z_{\odot}$. Right: Same of left panels considering the case of over abundance of Si and Al. Upper panels are for J01225+1339. Lower panels are for J02287+0002 considering z_{OI} . Coordinates and symbols are as for Fig. 5. The intersection point improves in certain cases, but in others is the same.

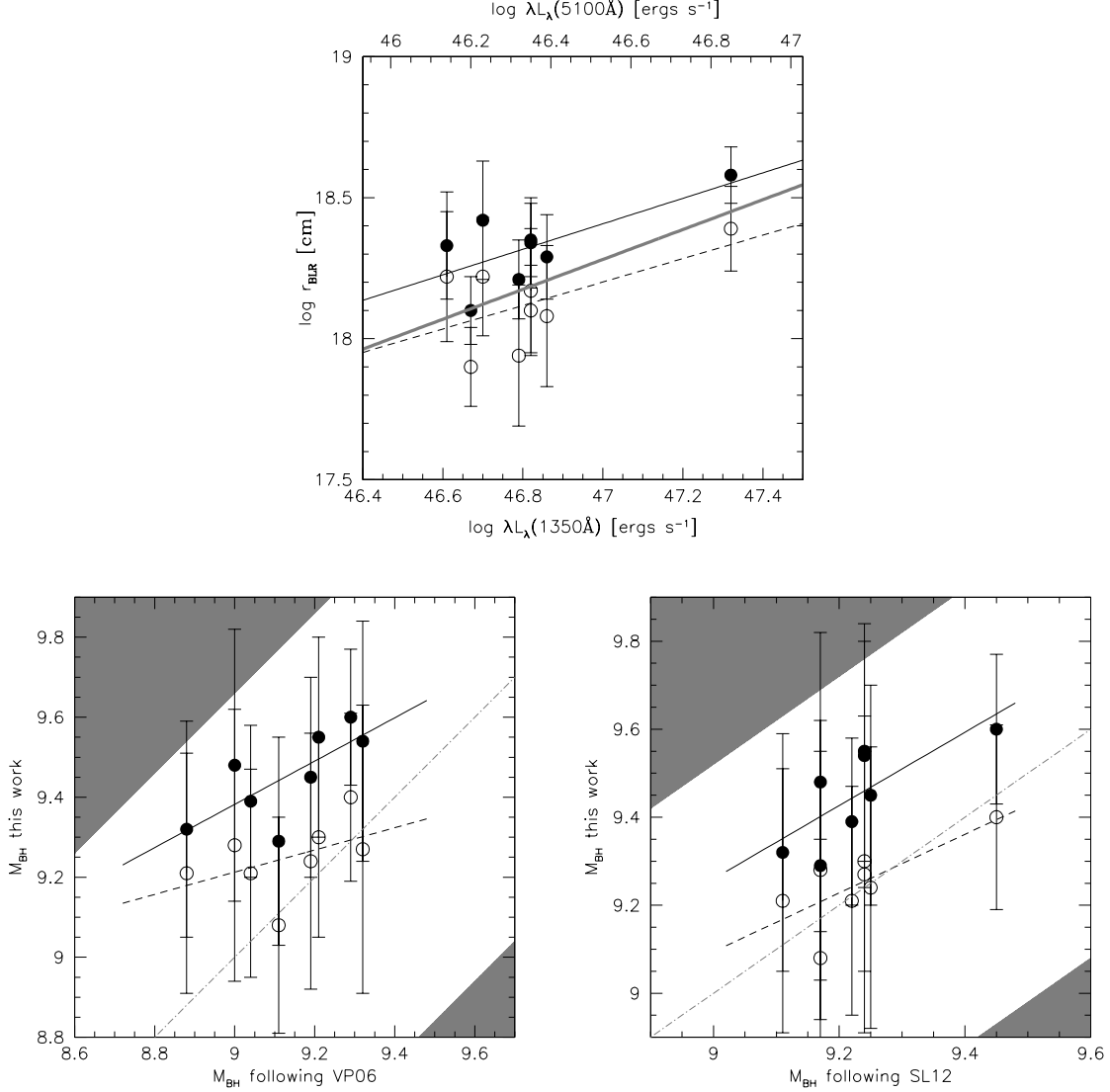


Fig. 7.— Upper panel: r_{BLR} estimates following the photoionization method with (open circles) and without (filled circles) correction for BLR low density/stratification, as a function of λL_{λ} measured at 1350\AA . The thick grey line is the $r_{\text{BLR}} - \lambda L_{\lambda}(5100\text{\AA})$ correlation as derived from Bentz et al. (2013). The continuous and dashed lines are unweighted least square fits to uncorrected and corrected data, respectively. $\log[\lambda L_{\lambda}(1350)/\lambda L_{\lambda}(5100)] \approx 0.47$, in accordance with typical SEDs of quasars (Elvis et al. 1994; Richards et al. 2006). Middle panel: M_{BH} comparison for the high- z sample. The shaded bands limit the 2σ confidence level spread expected on the basis of the Vestergaard & Peterson (2006) relation. The grey dot dashed line is the equality line. Filled symbols refer to uncorrected intensity ratios; open symbols are for intensity ratios corrected because of low-density emission. Bottom panel: same of middle panel, with M_{BH} computed from the Shen & Liu (2012) relation.